Quantifying the impact of early calcite cementation on the reservoir quality of carbonate rocks: a comparison of 2D and 3D process-based models

Quantifying the impact of early calcite cementation on the reservoir quality of carbonate rocks: a comparison of 2D and 3D process-based models

Hosa, Aleksandra[a,b,*], Wood, Rachel[a,b]

[a] *Grant Institute, School of GeoSciences, University of Edinburgh, King's Buildings, James Hutton Road, Edinburgh EH9 3FE, UK*
[b] *International Centre for Carbonate Reservoirs (ICCR)*

Abstract

The reservoir properties of carbonates are controlled both by deposition and diagenesis, and the latter includes early calcite cementation which can exert a strong control on the evolution of subsequent diagenetic pathways. Here we investigate early cement growth in grainstones to quantify the impact on evolving pore space and partially to examine trends in the relationships between cementation and permeability. We compare process-based models of early cementation in 2D (Calcite2D) and 3D (Calcite3D). Both models assume polycrystalline and monocrystalline grain types, upon which grow isopachous and syntaxial calcite cement types, respectively. We also model two common rhombohedral calcite forms: the blocky form $01\bar{1}2$ and elongated form $40\bar{4}1$.

Results demonstrate the effect of cement competition: an increasing proportion of monocrystalline grains creates stronger competition and a reduction in the impact of individual grains on the early calcite cement volume and porosity. Isopachous cement is effective in closing pore throats and limiting permeability, especially in the 2D model. We also show that the impact of syntaxial cement on porosity occlusion and therefore flow is highly dependent on monocrystalline grain location and direction of the grain crystal axis. This can lead to very different permeabilities in samples of the same porosity in both the 2D and 3D

*Hosa, Aleksandra
Email address: ola.hosa@ed.ac.uk (Hosa, Aleksandra)

results.

3D modelling shows that for samples with crystal form $01\bar{1}2$ at constant porosity, permeability becomes lower as the proportion of monocrystalline grains increase, although this impact is relatively minor. Samples with crystal form $40\bar{4}1$ produce inconclusive results.

Poroperm data generated by Calcite3D can be fitted with an exponential curve with a high coefficient of determination, as observed in natural media. This is in contrast to the 2D study, where the variability at any given porosity spans up to two orders of magnitude. Moreover, the clustering of Calcite2D model outputs with different widths of isopachous cement suggests that this cement type is a strong control on the permeability. Results of the 2D modelling ($0.01 - 8D$) are in reasonable agreement with measured permeability reported for grainstones ($0.1mD - 5D$) as well as for the plug data of the samples used in modelling (porosity $22 - 27\%$, permeability $0.2 - 3D$). Permeability results, however, at any given porosity have a wide range due to the bias inherent to the 2D flow modelling. Calcite3D is successful in modelling realistic changes in cement volumes and in the pore space morphology, but permeabilities ($0.01 - 30D$) are above the range reported due to very high permeability of the initial synthetic sediment deposit ($58.9D$).

These results illustrate that subtle differences in early carbonate diagenesis, such as the exact location and orientation of the crystal axes of the monocrystalline grains, can have significant impact on the properties of cemented rocks. We also highlight the importance of 3D, rather than 2D, digital rock modelling and flow simulation to obtain reliable rock properties predictions.

Keywords: Digital rock, Synthetic rock, Carbonates, Porous Media, Porosity, Permeability, Calcite cement, Isopachous cement, Syntaxial cement

---

1. Introduction

Carbonate rocks are complex, partially due to the heterogeneity of sediment grain types but also due to diagenesis, which can take many pathways leading

to a multitude of final rock types. Porosity and permeability loss in carbonates is due to mainly grain-to-grain chemical compaction (pressure solution), mechanical compaction and cementation. Pressure solution closes pore throats thus isolating pore bodies [1] and cementation can reduce pore throats as well as increases the surface area and tortuosity of pores. Mechanical compaction is the least effective process in reducing permeability relative to an incremental decrease in porosity, as permeability reduction is achieved mostly by a loss of porosity, increase in pore-throat lengths, and an increase in the tortuosity of flow paths due to closer grain packing [1].

Given the diversity of subsurface carbonate rocks, rock modelling at the pore scale has been widely used to predict reservoir rock properties such as absolute permeability, capillary pressure, and relative permeability. Synthetic rock models are flexible and considerably less expensive than data obtained via experiments. Importantly, such models can also be used to test hypotheses as to the impact of specific diagenetic events on evolving flow properties.

Few models, however, have been dedicated to carbonates and they have used either statistical reconstruction [2, 3, 4, 5] or process-based approach [6, 7, 8]. Most process-based models, however, capture only one specific type of carbonate or formation process [6, 7]. Nevertheless, these models report successful prediction of rock petrophysical properties within the range of experimental data.

1.1. Modelling Objectives

Although diverse, carbonate-hosted hydrocarbon reservoirs have a set of common cement types, which can be used to produce geologically-guided models of cementation. This study undertakes pore-scale rock modelling to quantify how early diagenetic calcite cements influence the physical properties (porosity and permeability) of carbonate rocks. Also explored is the role of initial carbonate sediment type in controlling the distribution of such early calcite cements, as grain crystallinity can act as a strong influence on the type of cement seeded [9]. This study focuses upon early marine cements in calcite-dominated grain-

stones, as such rocks can often have good reservoir quality (high permeability and producibility) [10, 11].

We consider two types of grains which develop different types of early calcite cement [10]; both are common in reservoir rocks. Syntaxial calcite cement, sometimes also called epitaxial [12], is associated exclusively with monocrystalline grains (single crystal), while isopachous cement is a common early marine cement that develops on polycrystalline grains (consisting of multiple, often sub-resolution crystals) [13]. We postulate that due to differences in the morphology of these cement forms, their relative proportion will have varying impacts on the evolution of pore space morphology and therefore on permeability.

In order to investigate the dependence of rock properties on sediment type, a pore-scale cementation modelling methodology is developed and implemented in both 2D and 3D. The model is object- and process-based and focuses on maintaining the geometries of isopachous and syntaxial cements. Processes modelled include cementation in both models and also deposition in the 3D implementation. The model aims to simulate cementation as it occurs in natural carbonates, taking into account the geometries of the developing cements, as well as such local phenomena such as grain-grain impact (or impingement). We use the model to generate multiple synthetic rock samples of varying sediment type, i.e. the ratio of monocrystalline and polycrystalline grains. The Lattice Boltzmann method is then utilised to quantify the permeability of these synthetic samples. The overall goal of this study is to establish *trends* in the evolution of permeability in carbonates with early cementation.

1.2. Crystallinity of Carbonate Grains and Early Calcite Cement Types

Lander et al. [9] demonstrated that the crystallinity of quartz grains influences the volume of cement developed around them. Monocrystalline grains tend to produce large volumes of syntaxial overgrowth while polycrystalline grains develop thinner isopachous fringes [14]. In addition to volume, these two types of cement have different geometries and so their impact on the morphology of pore space varies.

Most carbonate grain types are polycrystalline [14]. These include the majority of skeletal carbonates, as well as non-skeletal grains such as pellets and ooids. The surfaces of these grains can be described as a mosaic of seeding sites with different crystal axes orientations and thus they develop cement typical for polycrystalline grains [14].

Most monocrystalline carbonate grains are skeletal fragments of organisms belonging to the phylum Echinodermata (sea urchins, starfish, brittle stars, sea lilies and sea cucumbers). Calcareous remains of echinoderms rarely constitute more than 10% of modern sediment grains [14]. But in the past (especially in the Palaeozoic) they had much greater quantitative significance, in some cases even dominating the allochems [15].

The two types of early shallow marine calcite cements typical for grainstones considered in this study are isopachous cement and syntaxial cement or overgrowth (Figure 1). Syntaxial overgrowth is associated exclusively with grains that can be treated as monocrystalline, while isopachous cement occurrs around polycrystalline grains [15, 10, 16, 17, 18]. Early marine cementation occurs rapidly before significant compaction takes place. Syntaxial and isopachous cements are both volumetrically significant early marine calcite cements.

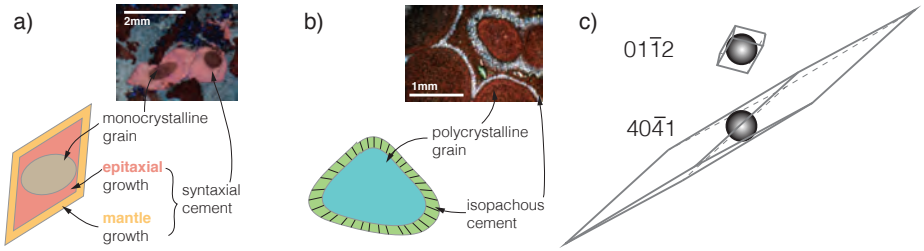

Figure 1: a) Thin section and model of a monocrystalline grain (brown) with syntaxial cement; red represents the epitaxial growth and orange represents concentric (mantle) growth. b) Thin section and model of isopachous calcite cement in a carbonate beachrock. c) Comparison of the shape and size of crystals of the rhombohedral crystal form 01$\bar{1}$2 and 40$\bar{4}$1 circumscribed on two spheres of the same size. The length of crystal form 40$\bar{4}$1 is 7.2 the length of form 01$\bar{1}$2 and the volume is 5.8 times bigger, however the volume of the cement (the volume of the rhombohedron diminished by the volume of the sphere) is 9.6 times greater in case 40$\bar{4}$1.

1.2.1. Syntaxial cement

Syntaxial cement seeds on a monocrystalline grain, most notably echinoderm fragments, and grows in optical continuity to it [14]. In a growing crystal, ions preferentially occupy the sites that result in greater release of energy. Non-euhedral faces of a grain provide a much greater release than euhedral faces [19]. As a result of this, calcite overgrowth proceeds rapidly until euhedral faces are achieved (epitaxial growth). Subsequently, the rate of growth decreases considerably (mantle/concentric growth) [20, 9] (Figure 1a). In the absence of any obstacles, monocrystalline grain grows rapidly until all faces are euhedral and the crystal form of calcite is achieved. As crystal forms of calcite are usually elongated, cement growth on a monocrystalline grain is asymmetric and depends on the orientation of the crystal axis of the grain. Once the euhedral faces of the growing crystal are reached, cement growth can continue in a form of mantle growth, often continuing into the burial zone [10].

1.2.2. Crystal forms of calcite

Calcite belongs to a trigonal hexagonal scalenohedral crystal system [21]. Over 800 different forms of calcite have been described, the most common of which are the rhombohedral and scalenohedral forms. This work focuses on the rhombohedral form, but even within this group many variations exist. Such variations include forms with Miller-Bravais indices $10\bar{1}1$, $40\bar{4}1$ and $01\bar{1}2$. The index $01\bar{1}2$ rhombohedron belongs to calcite forms most frequently observed in nature, and also the most commonly derived in the laboratory [22]. Another common rhombohedral form of calcite is $40\bar{4}1$ [20]. The main difference between these two rhombohedral forms is that $01\bar{1}2$ is more blocky and $40\bar{4}1$ is more elongated, which results in different volumes of syntaxial cement produced. Figure 1c illustrates that in the absence of any obstacles, rhombohedral crystal form $40\bar{4}1$ produces significantly greater volume of epitaxial overgrowth than crystal form $01\bar{1}2$ [20]. There are no quantitative studies on the abundance of the different crystal forms in the cement of carbonate rocks. Thus the approach in this work is to select crystal forms that are reported to be common ($01\bar{1}2$ and

$40\bar{4}1$, Figure 1c), and perform studies for each of these forms.

1.2.3. Isopachous cement

Isopachous cement develops on grains that do not have the capacity to seed a single crystal and form as fringes of either fibrous, bladed or microcrystalline crystals of nearly constant thickness around grains (Figure 1b) [10]. The thickness of the fringe is typically $20 - 100\mu m$ [17]. Isopachous cement is common in grainstones and is particularly typical in beachrock [23] (Figure 1b).

The crystals on the surface of the grain can be oriented in various directions, but those oriented normal to the substrate grow fastest and, as precipitation proceeds, they eliminate the crystals of other orientations [14]. In similarity to syntaxial cements, once euhedral faces are achieved, precipitation slows down considerably.

1.2.4. Impact of early cements on pore space morphology and permeability

Grain type plays an important role in determining the resulting pore space morphology of the final rock through the preferential development of cement type. The pore space of sediments composed predominantly of echinoderm fragments (monocrystalline grains) is likely to be completely occluded by syntaxial cements and permeability significantly reduced [10, 24]. In fabrics where monocrystalline grains are more sparse, cements tend to block local pore throats intermittently, creating a patchy cement distribution, and as such cementation may have a fairly low impact on porosity and permeability [25].

In contrast, isopachous cement often precipitates evenly around all polycrystalline grains, and so does not penetrate deep into intergrain pore spaces [10]. By its nature, isopachous cement narrows all pore throats and, depending on the thickness of isopachous fringes, can close off many pore throats, so significantly reducing pore connectivity and permeability.

1.2.5. Competition for growth space, impinging and 'shadow' effects

Due to the proximity of carbonate grains, syntaxial overgrowth almost always encounters other grains, which may or may not be developing syntaxial

overgrowths. Thus the full crystal shape of calcite is often never reached and euhedral faces overgrowths form compromise boundaries [26, 20]. The average volume of syntaxial cement per grain in a cemented rock is dictated by the competition during growth: the more monocrystalline grains there are that develop syntaxial overgrowth, the smaller the average volume of cement produced per grain.

During cement growth, grains are very likely to impinge on one another, and thus deactivate seeding sites and create compromise boundaries with other grains before reaching euhedral faces. Depending on the arrangement of the grains, impinging effects may lead to a 'shadow' effect (J.A.D. Dickson, pers. comm.), whereby once an obstacle is encountered during epitaxial growth, a portion of the seeding area on a non-euhedral face of the grain is blocked by it. As a result, no further syntaxial overgrowth will be seeded by that area (Figure 2). Syntaxial cement can therefore only grow to its full extent in the absence of other grains (Figure 2a). Once an obstacle is encountered, the seeding site of the growing cement that came in contact with the obstacle is blocked and the zone in the 'shadow' of the obstacle will not be produced. Fast epitaxial growth ceases and a smaller volume of cement is formed (Figure 2b).

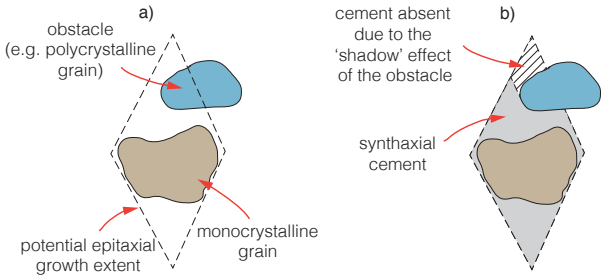

Figure 2: 'Shadow' effect of grains impinging on growing cement; a) extent of syntaxial overgrowth that would develop in the absence of obstacles, b) final cement geometry.

1.3. Modelling in this study

We propose a process-based and object-based model of calcite cementation with a stochastic initial condition. An implementation of this model is given

in 2D and in 3D: here termed Calcite2D and Calcite3D, respectively. The cementation model assumes static conditions, i.e. a supersaturated solution with respect to calcium carbonate, which is realistic for early marine diagenetic conditions, and concentrates on the geometries of the two types of early calcite cement typical for carbonates: syntaxial and isopachous (see Section 1.2).

In the initial stage of the cementation model, mono- and polycrystallinity is assigned to grains at random as are the crystal axes directions of the monocrystalline grains (initial condition). Next a geometric approach is followed: syntaxial cement is modelled by circumscribing (or decorating) the grains with a shape of one of two rhombohedral forms of calcite ($01\bar{1}2$ or $40\bar{4}1$) and isopachous cement is modelled by adding a layer of constant thickness around the grains. In the 2D study the structure on which cement is grown is an image of a natural carbonate reservoir rock that has been stripped of cement. In the 3D study the statistics of grain size and shape distribution serve to generate a 3D structure in a process-based model that mimics deposition.

Current 3D imaging methods, e.g. microcomputed tomography (μCT), do not differentiate between the grain and the cement, which is necessary before one can segment the image and analyse the original deposit. The grains are modelled as rigid bodies falling due to gravity and settling on one another in a 3D box using the collision physics of falling grains in an open-source Bullet Physics Library [27] employed in a Blender environment [28]. The model is flexible in terms of the shape and size distribution of grains, although in this application, the shapes are limited to convex ellipsoids.

The inspiration for the modelling work stems from Prism2D, a 2D model simulating sandstone diagenesis [9] which differentiates between monocrystalline and polycrystalline grains, to model accurate shapes of growing quartz crystals and to account for the effect of growing grains impinging on one another. Prism2D is physically-based as it employs a kinetic rate law to model the growth of cement, which is not the approach of this study. Here we follow a geometric approach, which focuses on recreation of shapes characteristic to calcite cements (see Section 1.2). Prism2D models crystal growth on euhedral as well as on

non-euhedral faces of the quartz crystal, while Calcite2D only models syntaxial cement on non-euhedral faces in the rapid epitaxial stage. Calcite2D, however, is fully flexible in terms of directionality of the crystal axes that monocrystalline grains can take, whereas Prism2D is limited to only four directions. Additionally, we model more than one type of cement to explore competition effects, and the model is implemented in 3D (Calcite3D) which enables better flow property prediction.

1.4. Flow simulation in 2D vs 3D

This work aims to provide insight into the permeability of porous media through two approaches: a high resolution and large scale 2D study and a lower resolution and smaller scale 3D study. After cemented synthetic samples are derived using Calcite2D and Calcite3D, flow is simulated using the Lattice Boltzmann (LB) method [29, 30, 31, 32, 33] in order to obtain absolute permeability.

Modelling permeability in 2D has limitations, the most significant of which is a loss of the impact that rock anisotropy has on permeability. This is not an issue in the work presented here, as carbonate grainstones, which are the focus here, are relatively isotropic. Another limitation of the 2D method is the loss of connectivity of pores in the 3^{rd} dimension, which affects permeability. As a result, some 2D model outputs found to have no percolation might actually have pore connectivity in the 3^{rd} dimension and a non-zero permeability.

Despite these disadvantages, 2D permeability studies are still performed [33, 34] as samples of larger sizes and higher resolutions can be afforded. Cemented synthetic samples used in Calcite2D are 2000^2 pixels with a pixel size of $5\mu m$. This is effectively an order of magnitude higher than that usually undertaken in 3D modelling. This sample size allows modelling of a large number of grains and maintains grains 'smoothness' (non-pixelation). Also, these model outputs are large enough to allow for in-sample heterogeneity, e.g. the presence of areas with varying porosity within one sample.

A major disadvantage of modelling permeability in 3D is the limitation of

sample size and resolution, as the computational cost scales with these. Most 3D rock modelling utilising LB simulations use samples of around 400^3 voxels [35, 36, 8, 37, 33, 38, 39]. Synthetic samples used in Calcite3D have a computational size of 300^3 voxels and voxels $10\mu m$ in size. Samples of such resolution are limited to a relatively small number of grains as well as to the accuracy of the pixel representation of the grains: in some cases thin pore throats are lost due to segmentation at a low resolution, which results in a loss of pore connectivity. All these factors influence the quality of permeability prediction.

2. Methodology

We introduce **Calcite2D** and **Calcite3D**, Matlab implementations of the process-based cementation model in 2D and 3D focusing on two early marine calcite cements: isopachous and syntaxial. Both implementations of the cementation model have two stages: Stage 1 defines the sediment type in terms of the ratio of monocrystalline to polycrystalline grains and the directions of the crystal axes of the monocrystalline grains; Stage 2 implements cement growth on both types of grains in a stepwise fashion - 1 pixel layer every iteration. Stage 1 is not computationally intensive but Stage 2 involves multiple iterations on a large matrix (the size of the porous medium) and was performed using the Edinburgh Compute and Data Facility ('Eddie') at the University of Edinburgh.

The processes taken into account in the models is cementation in both versions of the model and deposition in the 3D. In the 2D the process of deposition is not modelled as the methodology utilises a back-stripped thin-section image of a natural reservoir carbonate [2]. Calcite2D and Calcite3D take a geometric approach and focus on the recreation of shapes characteristic for calcite cementation. Syntaxial cement is only modelled on non-euhedral faces that occurs in the rapid epitaxial stage.

2.1. Overview of the 2D methodology

The 2D methodology starts with the treatment of the initial medium, followed by two stages of Calcite2D and finishes with a procedure to obtain the

absolute permeability using Lattice Boltzmann method (Figure 3). This procedure is used to create thousands of cemented synthetic samples for various ratios of monocrystalline and polycrystalline cements and for two different calcite crystal forms. Permeability is calculated only for a subset of all generated synthetic samples.

The 2D methodology starts with the segmentation and binarisation of a thin-section image that serves as an input to Calcite2D (a). In Stage 1 of Calcite2D, grains in the binary image are identified and a portion of them, chosen at random based on a model input, is labeled monocrystalline (b). For every monocrystalline grain, the crystal axis (c-axis) is defined, also chosen at random from all possible 3D orientations. In Stage 2 of Calcite2D, the cement is grown on all of the grains (c). The type of cement is determined by grain type, with syntaxial growth on the monocrystalline grains and isopachous cement on the polycrystalline grains. The permeability of the cemented rock is then obtained via a Lattice Boltzmann simulation (d). The details of all steps of this methodology are given in the following sections.

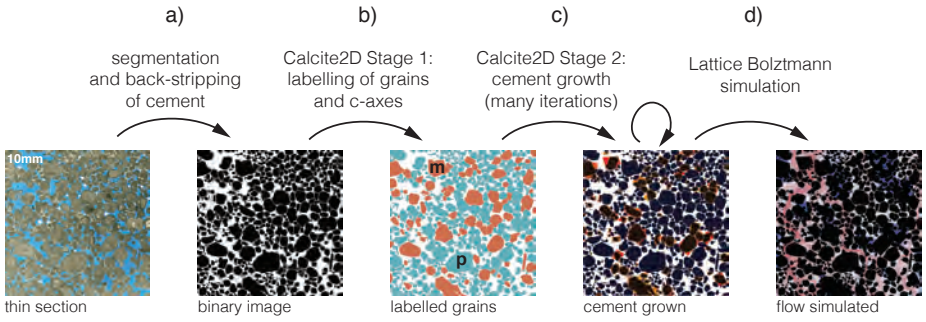

Figure 3: The methodology of the 2D cementation modelling; a) the thin-section image is segmented into pore, sediment and cement; cement is stripped and the image is binarised, b) Stage 1 of Calcite2D labels the grains as either monocrystalline (red, m) of polycrystalline (blue, p) and determines the directions of the crystal axes of the monocrystalline grains, c) Stage 2 of Calcite2D grows 1 pixel layer of cement every iteration until completion (reds - syntaxial cement, blues - isopachous cement), d) a Lattice Boltzmann simulation is performed on the final medium to obtain permeability.

2.1.1. Treatment of the 2D Porous Medium

To illustrate the capabilities of Calcite2D a thin-section image of a real carbonate grainstone reservoir rock with early calcite cements is chosen (Figure 3a). The steps in the procedure that lead from the original colour thin-section image (Figure 3a) to the binary image that is used as an input to the cementation model (Figure 3b) are as follows (details are given in Appendix A):

1. first-pass automatic segmentation;
2. manual adjustment in a graphics package;
3. image resizing (from 3779^2 to 2000^2 pixels);
4. grain separation (post-processing step 1);
5. fine grains removal (post-processing step 2).

Laboratory measurements are $\phi = 24.4\%$ and $\kappa = 4700mD$. Due to the heterogeneity of carbonates, and the fact that a thin-section image carries only 2D information, the properties of the specific 2D rock image that is used in the modelling (Figure 3a) are expected to be different. The porosity of the segmented thin-section with natural cement is remarkably close to these data: 23.7%. The permeability, however, is dramatically different, as the naturally cemented medium is found to be not percolating, which is equivalent to $0mD$.

2.1.2. Calcite2D

Calcite2D has two stages, each of which takes one input parameter (Figure 4). Stage 1 involves grain identification and labelling as either polycrystalline of monocrystalline based on the input parameter α_0 (Figure 4a) as well as definition of crystal axes direction and establishing of the polygonal bounds of epitaxial growth (Figure 4b). In the code, α_0 goes through a random number generator and the resulting portion of monocrystalline grains in the sample α may differ slightly from the input. Stage 2 of Calcite2D implements calcite growth and takes as the input parameter the target width of the isopachous cement that will coat all polycrystalline grains β (Figure 4c and d). The details of the implementation can be found in Appendix B.

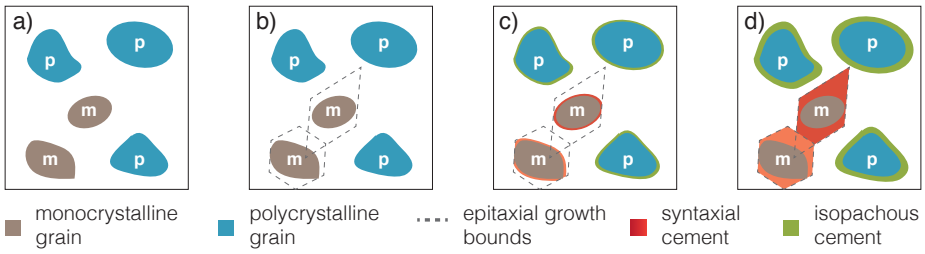

Figure 4: Steps of the Calcite2D implementation; a) detection of grains and labelling a portion of them monocrystalline based on the parameter α_0, b) establishing the outer bounds of the epitaxial growth for monocrystalline grains, c) growth of 1 pixel layer of cement around all grains; growth is prohibited outside of the epitaxial bounds, d) repetition of the addition of layers: for polycrystalline grains until the thickness of the isopachous cement fringes specified by the input parameter β is reached, for monocrystalline grains - until all bounding polygons are filled.

2.1.3. Example model output of Calcite2D

Figure 5 illustrates two cemented synthetic samples that are grown on the 2000^2 pixel porous medium (Figure 3b), one using the crystal form $01\bar{1}2$ (a) and the other using the crystal form $40\bar{4}1$ (b). Both images exhibit textures realistic for calcite cementation. As crystal from $40\bar{4}1$ is more elongated, there are more elongated forms of syntaxial cement present in the sample shown in Figure 5b than in Figure 5a. As the crystal form $40\bar{4}1$ leads to more elongated forms of syntaxial cement this results in more iterations necessary for the completion of Stage 2 of Calcite2D. The synthetic sample with crystal from $01\bar{1}2$ (Figure 5a) required 109 iterations, while the synthetic sample with crystal from $40\bar{4}1$ (Figure 5b) required 194 iterations until completion.

2.2. Overview of the 3D methodology

The methodology to create early calcite cement in a porous medium in 3D starts from the analysis of a 2D thin-section to obtain a distribution of grain characteristics. This is followed by the generation of the 3D porous medium based on these characteristics, and finally the two stages of Calcite3D and finishing with the procedure to obtain the absolute permeability using Lattice Boltzmann method. This methodology is used to create a single synthetic grainstone deposit, which is then used to generate thousands of cemented synthetic samples

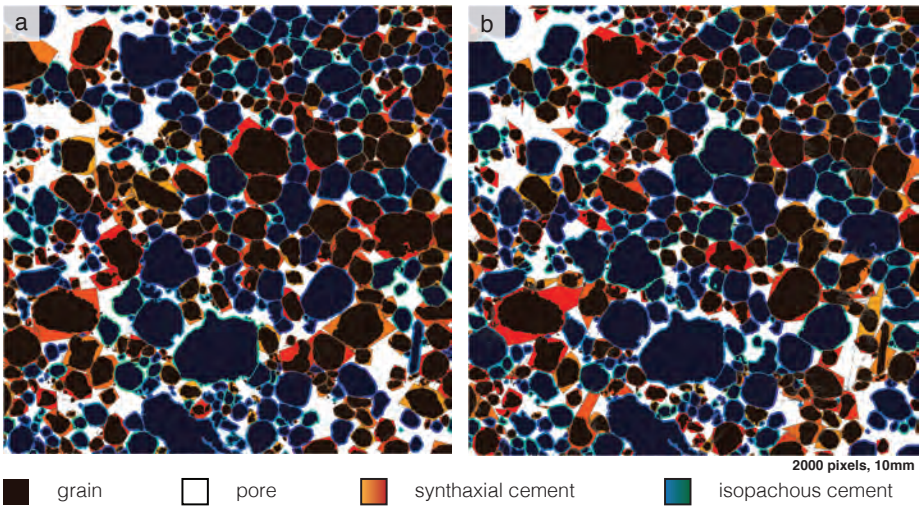

Figure 5: Model outputs of Calcite2D for both geometries of syntaxial cement with equal amounts of monocrystalline and polycrystalline grains in the sample ($\alpha_0 = 0.5$) and isopachous cement fringes of width $50\mu m$ ($\beta = 10 pixels$); a) crystal form $01\bar{1}2$, $\phi = 14.9\%$, b) crystal from $40\bar{4}1$, $\phi = 14.2\%$.

for various Calcite3D model input parameters (the content of monocrystalline grains and the width of the isopachous cement fringes) and for two different calcite crystal forms. 5946 cemented samples were generated using the crystal form $01\bar{1}2$, and 4086 samples were created using the crystal form $40\bar{4}1$.

Permeability was quantified for a subset of all generated synthetic samples (457 samples or 4.5%), with simulations performed on Archer, a UK National Supercomputing Service based around a Cray XC30 supercomputer.

Figure 6 shows the general steps in the cementation modelling methodology in 3D. This starts with the segmentation and the binarisation of a thin-section image and the extraction of a joint distribution of grain shapes and sizes. This distribution is used to create a packing of 3D grains in a process-based simulation that mimics the grains falling and setting due to gravity. The packing of grains is then cropped and voxelised to prepare as an input to the cementation model Calcite3D. In Stage 1 of Calcite3D, grains are randomly labelled as either monocrystalline or polycrystalline, based on a model input parameter. For every monocrystalline grain the crystal axis (c-axis) is defined, and chosen at

random from all possible 3D orientations. In Stage 2 of Calcite3D, the cement is grown on all of the grains. As in Calcite2D, the type of cement is determined by the grain type, with the syntaxial cement growth on the monocrystalline grains and the isopachous cement growth on the polycrystalline grains. The permeability of the cemented rock is then obtained via the Lattice Boltzmann simulation. Below, the details of all the steps of this methodology are given.

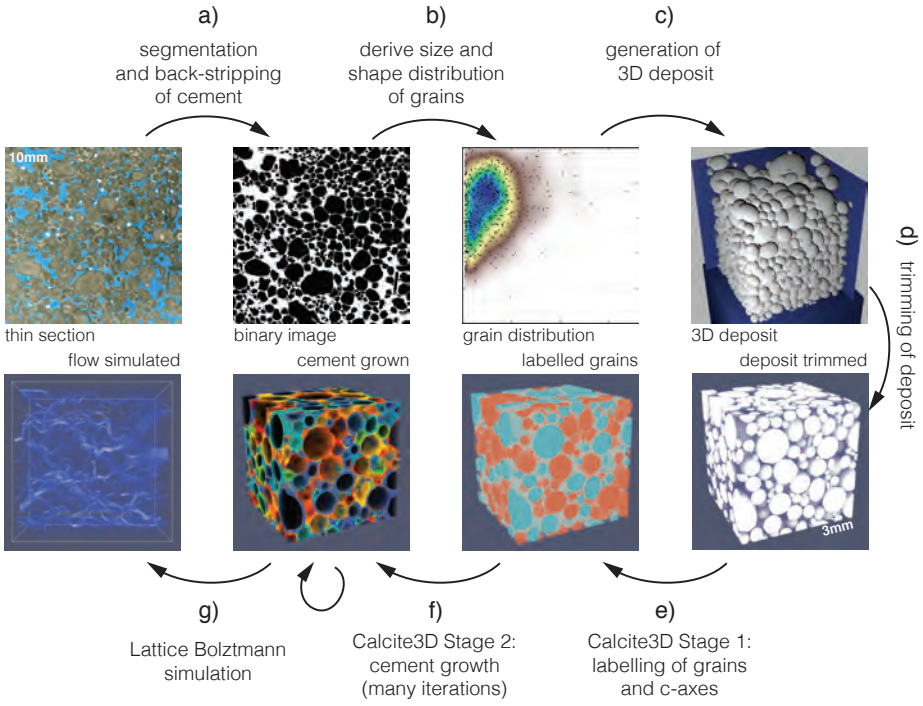

Figure 6: The general Calcite3D methodology: a) a thin-section image is segmented and stripped of cement, b) the joint distribution of grain size (the equivalent diameter) and shape (the aspect ratio of a fitted ellipse) is determined, c) the synthetic 3D deposit is generated based on that distribution, d) the synthetic deposit is cropped to avoid artefacts in grain arrangement due to box boundaries, e) Calcite3D, Stage 1: grains are labelled monocrystalline or polycrystalline and the crystal axes of the monocrystalline grains are determined, f) Calcite3D, Stage 2: the cement growth, g) the Lattice Boltzmann simulation of flow.

2.2.1. Generation of a 3D Porous Medium

To make the cementation model more realistic and versatile, the initial structure of the carbonate sediment should be close to the real carbonate deposit. To this end, a 2D thin-section image and the data extracted from it are used

to generate a synthetic 3D deposit that serves as an input to the cementation model Calcite3D.

The proposed methodology is process-based and follows similar published models, such as the work of Bakke and Øren [40]. The grain size and the shape distributions are extracted from a thin-section image of a real carbonate reservoir rock and used to generate a distribution of grains that are simulated to fall and settle under gravity. The details of the methodology can be found in Appendix C.

2.2.2. Comparison of the characteristics of the synthetic 3D deposit with the 2D thin-section

To allow comparison of the shapes and sizes of grains of the 3D medium with the original 2D data, 30 sections spaced every 10 voxel ($100\mu m$) are taken through the 300^3 voxel synthetic deposit. To avoid any bias in the shapes and sizes of grains due to image boundaries, only grains completely visible in these sections are considered, which amounts to 1412 grains. Figure 7b shows the resulting distribution and probability density function of these two variables.

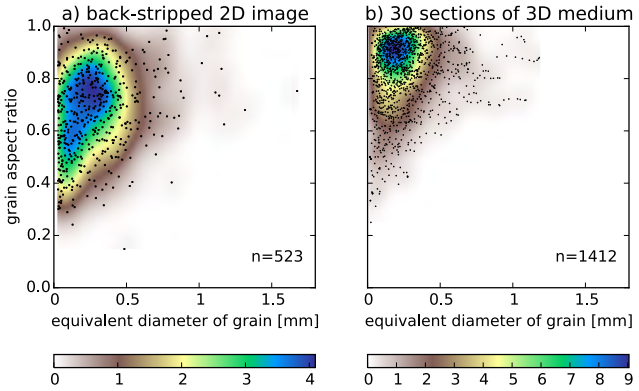

Figure 7: The joint distributions for grain size and shape for a) 523 complete grains visible in the binary back-stripped image, b) 1412 complete grains visible in 30 sections spaced every 10 voxels ($10\mu m$) though the 300^3 voxel synthetic deposit.

After analysing all possible 900 sections through the synthetic deposit in all three directions, the largest grain in the 3D medium was found to have a major

axis 1.3mm long. Since the sections through the medium are taken at 0.1mm intervals, inevitably some of the bigger grains are considered more than once (Figure 7b) as manifested by the patterns of the trailing points in the large grain range (around 1mm) in the centre of the image, which represent a single large grain appearing in multiple sections. Ideally each grain would be represented in the distribution only once. But to accomplish this, far fewer sections would need to be taken (no more than three), which would yield too few grains to be statistically sound.

The mean size of grain in the back-stripped medium is $286\mu m$, while the mean size in the 3D medium is $260\mu m$. The porosities of the two media are also very similar: the 2D medium has a porosity of 36.31% and the 3D medium has a slightly higher porosity of 37.91%. We conclude that this method of generating a 3D deposit is equally successful in reproducing grain sizes and porosity.

The method is less successful, however, in terms of the reproduction of grain shapes. The joint distribution of shapes and sizes found in the 30 sections through the 3D medium (Figure 7b) are not in good agreement in terms of the shape of the grains with the distribution derived from the 2D image (Figure 7a). The mean eccentricity of grains in the 2D image is 0.67 while the mean eccentricity of the cross-sections of grains in the 30 sections of the 3D medium is 0.82.

2.2.3. Calcite3D

The cementation methodology implemented in Calcite3D is very similar to the one implemented in Calcite2D. The main difference is that here the bounding polyhedra of the potential syntaxial cement are represented in the voxel form, i.e. a set of voxels in the bounding polyhedron for each monocrystalline grain is retained as a grain property and modified along the course of the simulation due to impinging effects. This leads to greater memory requirements as well as to longer time-to-solution.

Calcite3D has two stages, each of which takes one model input parameter. The overall steps of Calcite3D implementation are equivalent to the stages of

Calcite2D (Figure 4). The details of the implementation can be found in Appendix D.

2.2.4. Example model output of Calcite3D

Figure 8 shows model outputs of Calcite3D. The simulation of the sample with the crystal form $01\bar{1}2$ (a) took 32 steps and 2.1h to complete, but the simulation with the crystal form $40\bar{4}1$ took 85 steps and 13.0h to complete because the crystal form $40\bar{4}1$ produces more elongated syntaxial cement forms.

In both synthetic samples, cement is present that has grown into the plane of the section, even though the grain that seeded that cement is not present in that section. This applies to both isopachous (blue-green) and syntaxial (red-yellow) cements (Figure 8b). This is an improvement over the 2D model, where this phenomenon is not taken into account. 'Shadow' effects of impinging grains can also be observed in a couple of syntaxial cements present in the synthetic samples.

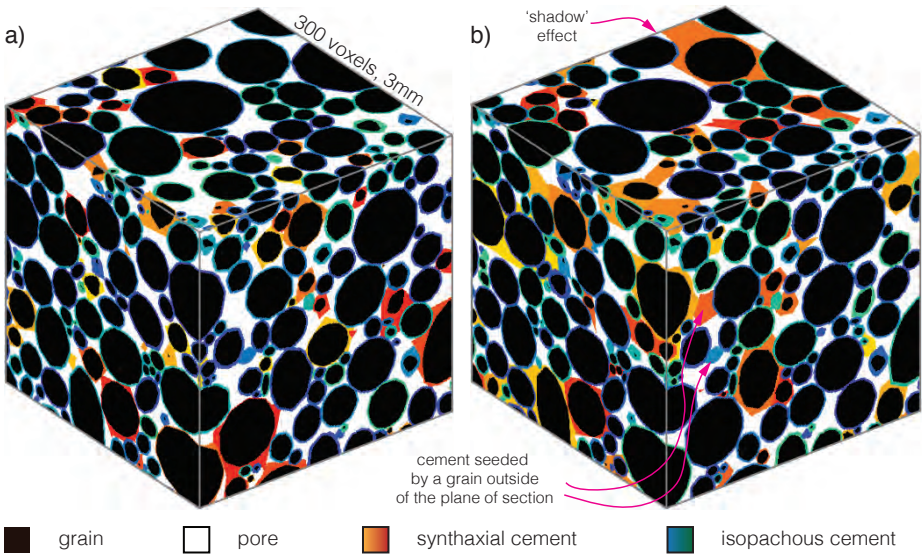

Figure 8: Model outputs of Calcite3D a) for the crystal form $01\bar{1}2$, $\alpha = 23.2\%$, $\beta = 2$ voxel, $\phi = 20.8\%$ b) for the crystal form $40\bar{4}1$, $\alpha = 18.7\%$, $\beta = 2$ voxel, $\phi = 16.2\%$.

2.3. Permeability Prediction Using Lattice Boltzmann Method

In order to quantify the absolute permeability of the model outputs of Calcite2D, a 2D version of the Lattice Boltzmann code (D2Q9) DL_MESO is used to simulate the flow through the synthetic media. A 3D version of the Lattice Boltzmann code (D3Q27) DL_MESO is utilised in the 3D study. DL_MESO was developed under the auspices of the Engineering and Physical Sciences Research Council (EPSRC) for the EPSRC's Collaborative Computational Project for the Computer Simulation of Condensed Phases (CCP5) [41]. Overall, 457 simulations were performed on Archer, a UK National Supercomputing Service based around a Cray XC30 supercomputer. The details of the simulation set-up can be found in Appendix E and of the calculation of permeability in Appendix F.

3. Results

Results are presented in terms of several quantities of interest (Table 1): the content of monocrystalline grains in the sample by volume (α), which is controlled by the model input parameter (α_0), the second model input parameter: the width of the isopachous cement fringes in pixels (β), porosity (ϕ) and permeability (κ).

3.1. Generated synthetic samples in 2D and 3D

Calcite2D and Calcite3D are used to generate multiple synthetic samples of varying content of monocrystalline grains (α_0) and varying width of the isopachous cement fringes (β). Two geometries of syntaxial cement are investigated: one that occurs if it is assumed that all monocrystalline grains develop a syntaxial cement of the rhombohedral the crystal form $01\bar{1}2$ and another one when the crystal form $40\bar{4}1$ is assumed. For both crystal forms, in the 2D study a total of 6959 cemented synthetic samples are generated with input parameter values for the content of monocrystalline grains α_0 ranging from 0 to 100% and for the width of the isopachous cement fringes β ranging from 0 to 10 pixels

Table 1: Quantities of interest.

Name	Definition	Unit
α_0	Stage 1 Calcite2D and Calcite3D input parameter: the target content of monocrystalline grains in a synthetic sample	%
β	Stage 2 Calcite2D and Calcite3D input parameter: the target width of the isopachous cement fringes	2D: pixel ($5\mu m$), 3D: voxel ($10\mu m$)
α	content of monocrystalline grains by volume (actually the area of the grain cross-section in the 2D study)	%
ϕ	porosity	%
κ	permeability	mD

(representing 0 to $50\mu m$) (Figure 9a). In the 3D study 5946 cemented synthetic samples are generated using the crystal form $01\bar{1}2$, with model input parameter values for the content of the monocrystalline grains (α_0) ranging from 0 to 100% and for the width of the isopachous cement fringes (β) ranging from 0 to 5 voxels (representing 0 to $50\mu m$) (Figure 9b), and 4086 samples using the crystal form $40\bar{4}1$.

In order to save simulation time and data storage space, each of the outputs of Stage 1 of Calcite2D is used to produce 11 cemented synthetic samples, each one with a different input parameter for the width of the isopachous cement fringes (β) in Stage 2 of Calcite2D. In the 3D study, each of the outputs of Stage 1 of Calcite3D is used to produce six cemented synthetic samples, with the width of the isopachous cement fringes (β) ranging form 0 to 5, in Stage 2 of Calcite3D.

The monocrystalline grain content α_0 passes through a random number generator, and so the final the monocrystalline grain content in the sample by number of grains (α) may differ slightly from the input parameter α_0. In the 2D, the only percolating synthetic samples are generated for the width of the

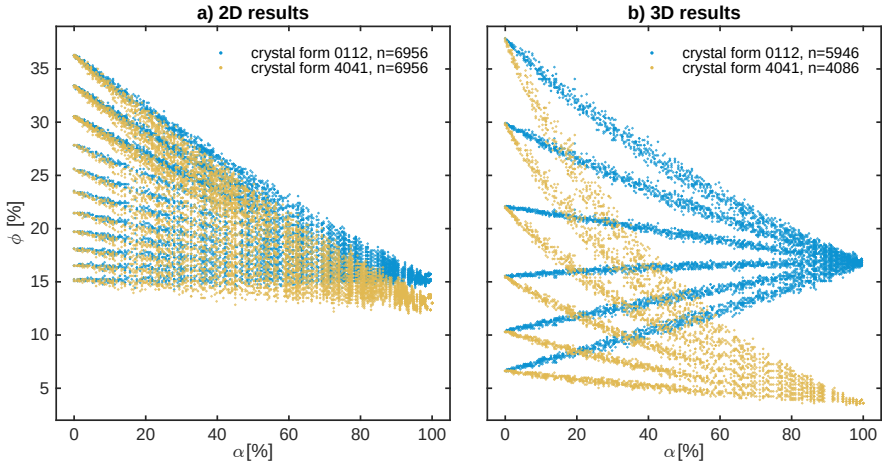

Figure 9: A comparison between the porosity of the synthetic samples produced with the crystal form $01\bar{1}2$ (blue) and $40\bar{4}1$ (yellow) for the results of the 2D (a) and 3D (b) studies.

isopachous cement fringes smaller than 3 pixels (representing $15\mu m$) and the monocrystalline grains content less than 60%, while in the 3D all synthetic samples generated using the crystal form $01\bar{1}2$ are percolating and only 13 of the synthetic samples generated using the crystal form $40\bar{4}1$ are not percolating.

3.1.1. Two crystal forms of calcite

The porosity in the case of the crystal form $01\bar{1}2$ is generally higher for synthetic samples of the same monocrystalline grain content by volume (α) than in the case of $40\bar{4}1$ (Figure 9). The crystal form $40\bar{4}1$ produces synthetic samples with lower porosity, and the difference between the results associated with the crystal form $01\bar{1}2$ and $40\bar{4}1$ increases with increasing content of the monocrystalline grains. In the 2D results, for high monocrystalline content samples, the porosity of the synthetic samples generated using the crystal form $01\bar{1}2$ converges to about 16% and the porosity of the synthetic samples generated using the crystal form $40\bar{4}1$ converges to about 13%, while these values in the 3D results are 17% and 4%, respectively.

This is further illustrated in Figures 10 and 11, which show the model outputs

generated using the crystal form $01\bar{1}2$ (a, b) and using the crystal form $40\bar{4}1$ (c, d) for the 2D and 3D, respectively. In the high monocrystalline content synthetic samples, the porosity of the samples with the crystal form $01\bar{1}2$ is around 15.5% in the 2D and 17% in the 3D and the porosity of the samples with the crystal form $40\bar{4}1$ is around 13.0% in the 2D and 4% in the 3D. Since there are so few polycrystalline grains, the width of the isopachous cement fringes does not significantly affect porosity.

Figures 10 and 11 also demonstrate that the crystal form $40\bar{4}1$ is much more effective in occluding the pore space than the crystal form $01\bar{1}2$. The elongated shape of the crystal form $40\bar{4}1$ causes syntaxial cement growth deep into the pore space, while the more blocky crystal form $01\bar{1}2$ produces a smaller volume of cement that occupies less pore volume.

3.2. Impact of Monocrystalline Grains on Cement Growth and Porosity

The volume of cement and the porosity of a synthetic sample cannot be accurately determined a priori, before the cement growth simulation is complete (Stage 2 of Calcite2D or Calcite3D). This is because even if the shape of the bounding polygons or polyhedra is known, the dynamics of the impinging cements and the creation of the compromise boundaries in the course of the cement growth can alter these pre-determined shapes. The following sections present the relationship between three quantities: the porosity (ϕ) and the monocrystalline grains content by volume (α).

3.3. Impact on porosity (ϕ vs α)

Figure 12 shows the porosity of all generated synthetic samples as a function of the monocrystalline grain content. The colour gradient in the direction parallel to the y-axis suggests that there is a strong dependence of the porosity on the amount of the isopachous cement in the sample.

In the 2D study the curves in all cases are decreasing and concave upward (Figure 12a and b). In the 3D all curves in the case of $40\bar{4}1$ are decreasing and they become progressively more linear for larger β (Figure 12d). Three

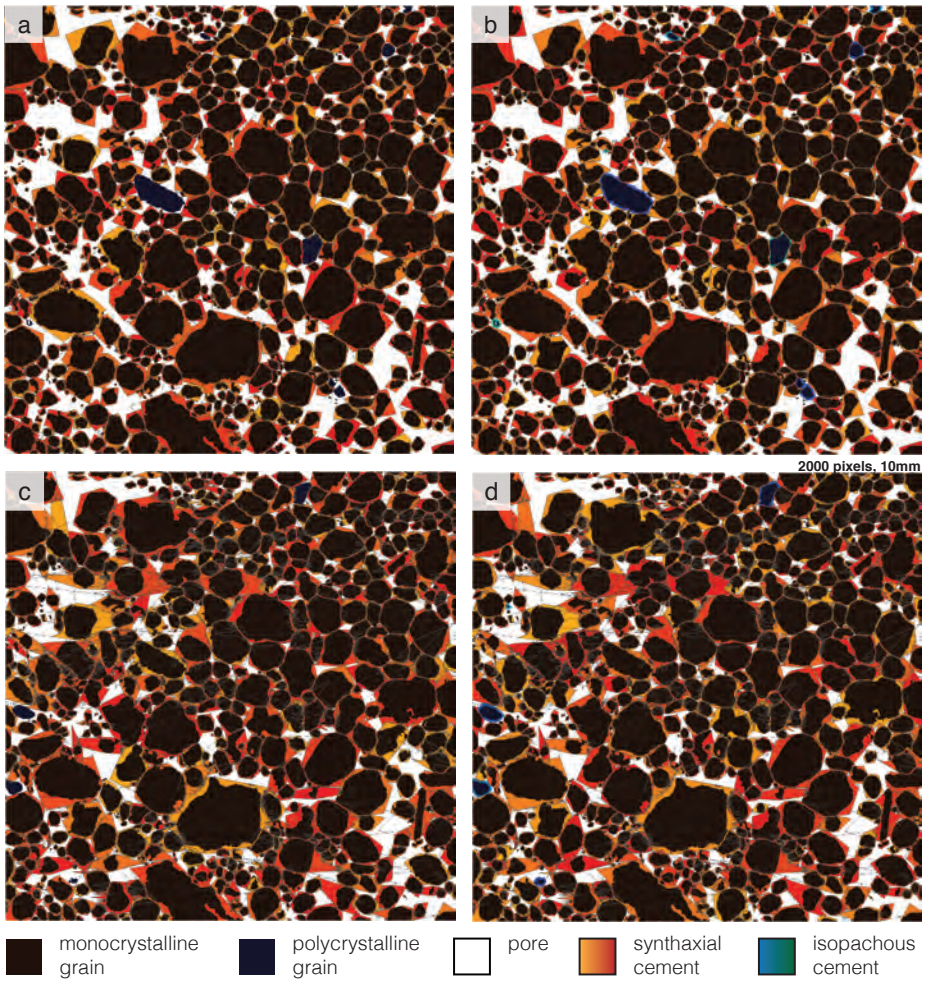

Figure 10: Calcite2D model outputs with a very high monocrystalline grain content for both crystal forms $01\bar{1}2$ (a, b) and $40\bar{4}1$ (c, d) with no isopachous cement (a, c) and 10 pixel ($50\mu m$) width of the isopachous cement fringes (b, d). The properties of each synthetic sample are as follows: a) $\phi = 15.8\%$, $\alpha = 98.5\%$; b) $\phi = 15.5\%$, $\alpha = 98.5\%$; c) $\phi = 13.1\%$, $\alpha = 99.9\%$; c) $\phi = 13.0\%$, $\alpha = 99.9\%$.

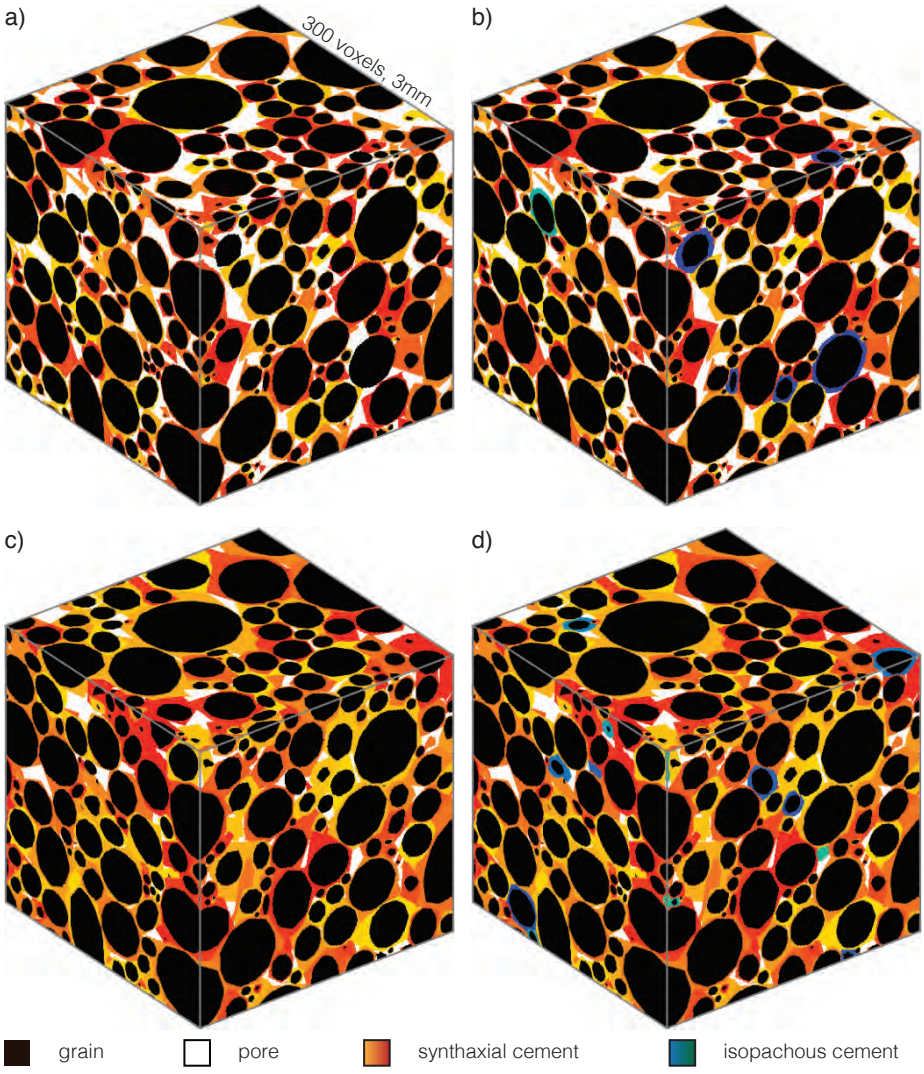

Figure 11: Very high monocrystalline grain content samples for both crystal forms $01\bar{1}2$ (a, b) and $40\bar{4}1$ (c, d) with no isopachous cement (a, c) and 5 voxel ($50\mu m$) width of the isopachous cement fringes (b, d). The properties of each sample are as follows: a) $\phi = 17.4\%$, $\alpha = 96.0\%$; b) $\phi = 16.4\%$, $\alpha = 96.0\%$; c) $\phi = 4.0\%$, $\alpha = 96.0\%$; c) $\phi = 3.6\%$, $\alpha = 96.0\%$.

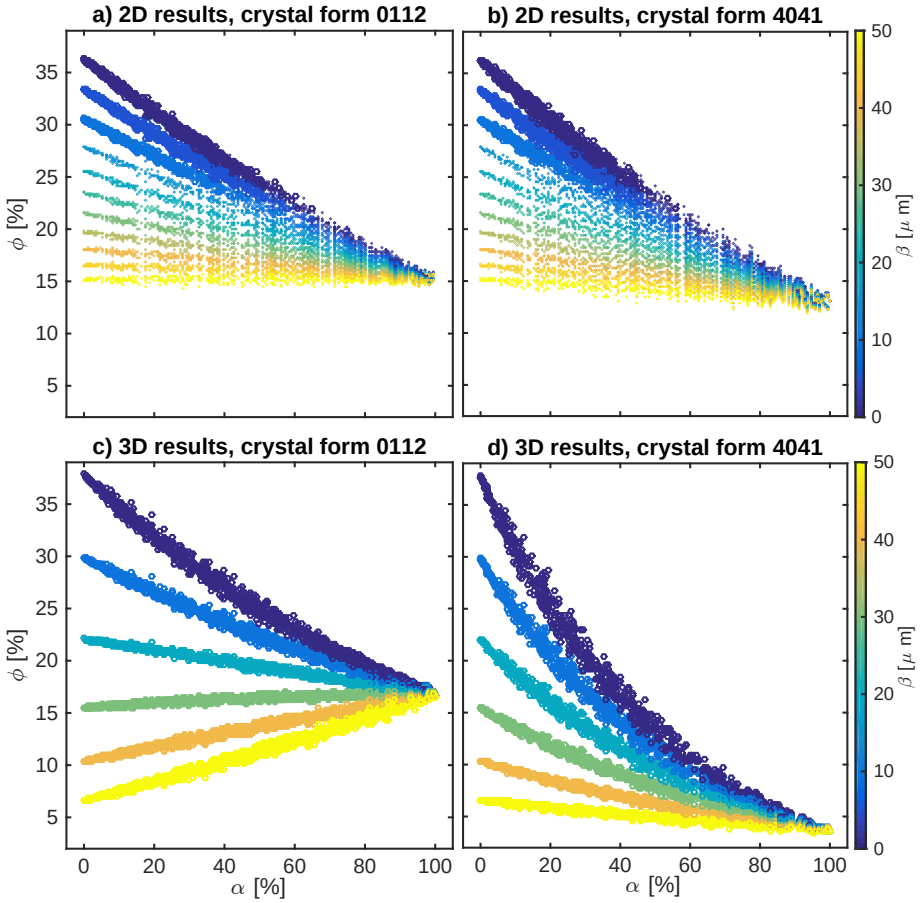

Figure 12: Porosity ϕ vs the monocrystalline grain content in the sample by volume α for synthetic samples with the crystal form $01\bar{1}2$ (a, c) and $40\bar{4}1$ (b, d) for the 2D (a, b) and the 3D (c, d) studies. The circles denote the percolating synthetic samples and the dots - non-percolating ones. The colours correspond to different values of the width of the isopachous cement fringes in the sample β: from blue ($0\mu m$) through to yellow ($50\mu m$).

decreasing curves in the case of $01\bar{1}2$, with $\beta = 0$, 1 and 2 voxels, are concave upward (Figure 12c) . It is notable that not all curves are decreasing for greater values of α, as is the case in the 2D study. The curves for $\beta = 3$, 4 and 5 voxels in the case of $01\bar{1}2$ are increasing and are concave downward.

3.4. Impact on Permeability

The choice of the cemented samples for the flow simulation is made from the pool of all percolating samples. In the 2D this includes 1636 synthetic samples in the case of the samples with the crystal form $01\bar{1}2$ and 1331 samples in the case of $40\bar{4}1$. Only the samples with very thin isopachous cement fringes ($\beta =$ 0, 1 and 2 pixels) are found percolating. In the 3D all 5946 synthetic samples in the case of $01\bar{1}2$ and 4073 synthetic samples in the case of $40\bar{4}1$ are percolating.

The primary strategy for selecting samples for the LB simulation involves targeting synthetic samples at specific porosities. That way, the impact of the monocrystalline grains content (α) on the permeability (κ) for samples of equal porosity (ϕ) can be investigated. For each of the targeted porosities, at least eight and preferably ten samples are selected from groups of samples with different widths of isopachous fringes (β).

In the 2D study the choice of the porosity values is made based on the availability of the synthetic samples within a 0.1% tolerance range of the targeted porosity, optimised for a uniform interval between the targeted porosities. The same six porosity values are targeted in both crystal form cases: 25.6, 26.4, 27.4, 28.4, 29.6 and 30.5%. Depending on the availability of synthetic samples, the number of the samples selected for the LB simulation for each of these porosities varies between 16 and 30 samples.

In the 3D the choice of these porosity values is made based on the availability of samples within a 0.2% tolerance range of a targeted porosity optimised for a uniform interval between the targeted porosities. Six porosity values are targeted in the case of the crystal form $01\bar{1}2$: 12.3, 15.5, 17.1, 20.8, 24.7 and 28.2%. Since not enough synthetic samples with porosity 24.7% are available in the case of $40\bar{4}1$, this porosity value is substituted with 25.2%, so that the

six porosities targeted in the case of the crystal form $40\bar{4}1$ are: 12.3, 15.5, 17.1, 20.8, 15.2 and 28.2%. Depending on availability, the number of synthetic samples selected for the LB simulation for each of these porosities varies between 20 and 40. In the case of $01\bar{1}2$, most of the targeted porosities offer only two groups with different width of the isopachous cement fringes, and only at porosities 15.5 and 20.8% three groups are available. In the case of $40\bar{4}1$, due to the decreasing nature of the ϕ-α curves, the number of available groups increases with decreasing porosity, from two groups at a porosity 28.2%, to four groups at a porosity 12.3%. The number of samples selected for the LB simulation in the case of $40\bar{4}1$ is larger due to the increased availability of samples.

The secondary motivation for selecting samples for the LB simulation is to cover the full range of the percolating synthetic dataset. For that purpose, in the 2D porosities spaced every 1% are targeted and the samples with the highest and the lowest value of the monocrystalline content (α) are selected for the three values of β, for which percolating samples are available (0, 1 and 2 pixels). This way a maximum of six synthetic samples are picked for each targeted porosity. In the 3D porosities from 5% to 30.5% spaced roughly every 1.5% are targeted and samples with the highest and the lowest value of the monocrystalline content (α) are selected from each group of the synthetic samples which have the same width of the isopachous cement fringes (β) available at any given porosity.

3.4.1. Impact of porosity on permeability (κ vs ϕ)

In 2D a slight trend of the logarithmic permeability increasing with the porosity is observed in the poroperm data for the synthetic samples of both crystal forms of syntaxial cement (Figure 13a and b), especially in the case of the samples with $\beta = 0$ and 1. Samples with $\beta = 2$ are grouped in the low permeability zone. This illustrates the impact of isopachous cement on permeability. The gradient of colour in Figure 13a and b, from blue in the bottom-right corner to yellow in the top-left corner of the plot, suggests a dependance of the permeability on the monocrystalline grains content in the sample (α). In this figure, however, this effect is not easy to isolate as it is 'contaminated' by the

effect that the porosity has on the permeability.

In 3D a clear trend of the permeability increasing with the porosity is observed for the synthetic samples of both crystal forms of syntaxial cement (Figure 13c and d), and this can be fitted with an exponential function. In the case of $01\bar{1}2$ there is a gradient of colour parallel to the y-axis, and samples with low a monocrystalline grain content (α) have generally higher permeabilities. The results in the case of $40\bar{4}1$ are inconclusive as there is no clear dependence of the permeability on the monocrystalline grain content.

3.4.2. Impact of monocrystalline grains content on permeability (κ vs α)

Permeability decreases for a larger content of monocrystalline grains (α) samples derived with Calcite2D (Figures 14a and b). This trend is particularly clear with varying width of the isopachous cement fringes (β).

In Calcite3D, in the case of $01\bar{1}2$, the permeability decreases with the monocrystalline grains content (α) only for synthetic samples with a low content of isopachous cement, and increases for samples with a higher content of isopachous cement, e.g. where $\beta = 5$ (Figure 14 c and d). The permeability of the high monocrystalline content samples converges to a value of about $3000mD$. In the case of $40\bar{4}1$, the permeability decreases for larger contents of monocrystalline grains (α). This trend is particularly clear in the results showing the impact of different widths of the isopachous cement fringes (β).

In both 2D and 3D the gradient of colour, from magenta in the top-left corner to light blue in the bottom-right corner of the plot, suggests dependence of permeability on porosity.

4. Discussion

We proceed to interpret and discuss the results presented in the previous sections highlighting the similarities and differences to the results of the 2D and the 3D modelling, followed by the discussion of the methodologies.

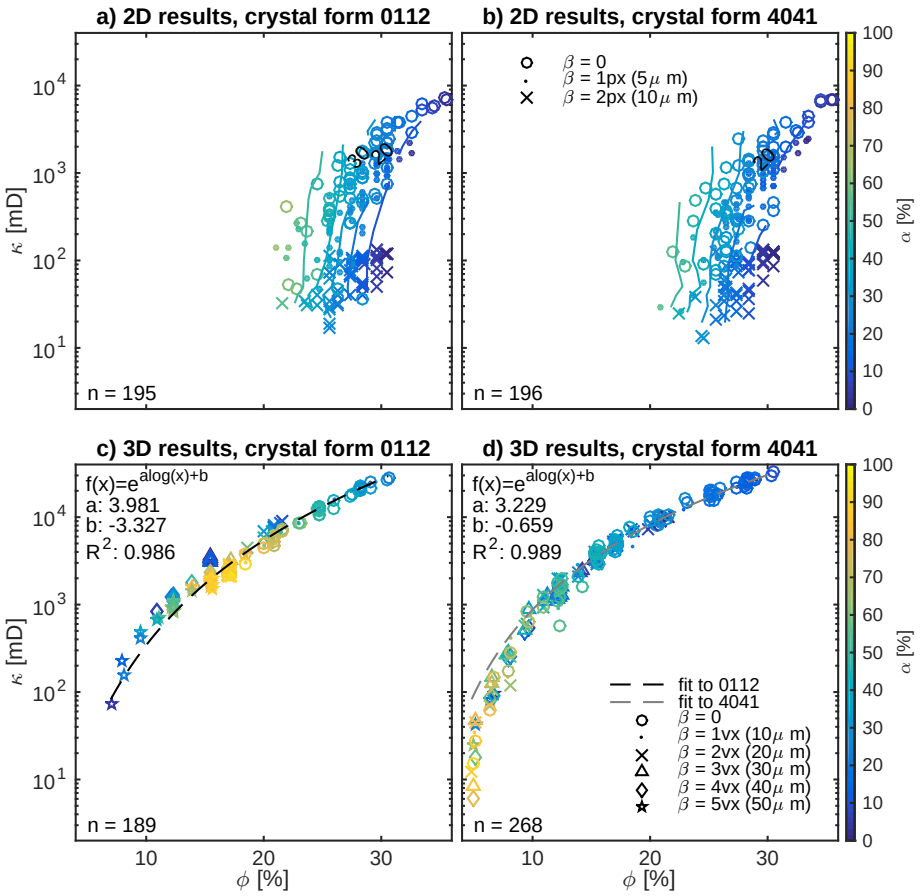

Figure 13: The permeability (κ) on a logarithmic scale vs the porosity (ϕ) for the synthetic samples with the crystal form $01\bar{1}2$ (a, c) and $40\bar{4}1$ (b, d) in the 2D (a, b) and the 3D (c, d) studies. Different symbols denote samples with a different width of the isopachous cement fringes. In the 2D results circles, dots, crosses represent samples with 0 voxels, 1 pixel ($5\mu m$) and 2 pixels ($10\mu m$) width of the isopachous cement fringes. In the 3D results, circles, dots, crosses, triangles, diamonds and stars represent samples with 0 voxels, 1 voxel ($10\mu m$), 2 voxels ($20\mu m$), 3 voxels ($30\mu m$), 4 voxels ($40\mu m$) and 5 voxels ($50\mu m$) width of the isopachous cement fringes, respectively. The synthetic data are coloured by the monocrystalline grains content in the sample by volume (α) from dark blue (low content) to yellow (high content). The 3D results are fitted with a curve of the form: $\kappa(\phi) = e^{a \cdot log(\phi)+b}$.

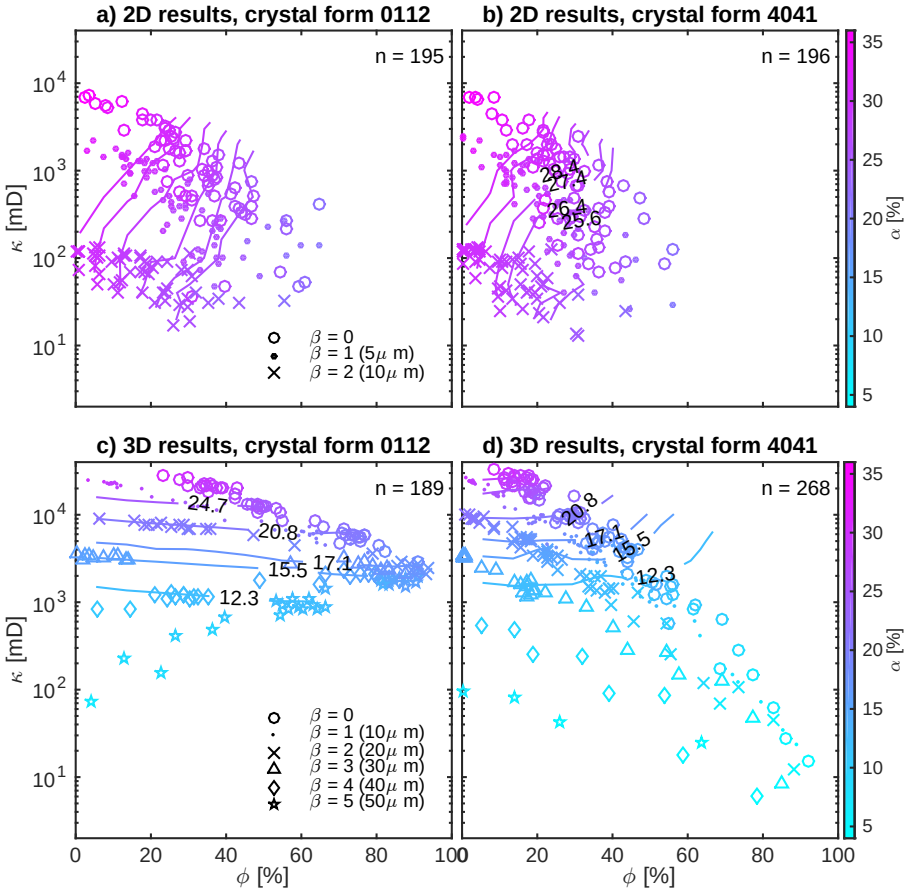

Figure 14: The permeability (κ) on a logarithmic scale vs the monocrystalline grain content by volume (α) for the synthetic samples with the crystal form $01\bar{1}2$ (a, c) and $40\bar{4}1$ (b, d) for the 2D (a, b) and the 3D study (c, d). In the 2D results the circles denote the synthetic samples with no isopachous cement, the dots - samples with 1 pixel width of the isopachous cement fringes, and x - samples with 2 pixels of the isopachous cement fringes. In the 3D results circles, dots, crosses, triangles, diamonds and stars represent samples with 0 voxels, 1 voxel ($10\mu m$), 2 voxels ($20\mu m$), 3 voxels ($30\mu m$), 4 voxels ($40\mu m$) and 5 voxels ($50\mu m$) width of the isopachous cement fringes, respectively. The synthetic data are coloured by porosity (ϕ), from light blue (low porosity) to magenta (high porosity).

4.1. Differences in the results between crystal form $01\bar{1}2$ *and* $40\bar{4}1$

The two crystal forms modelled differ in terms of shape and volume, so the results for synthetic samples produced using these crystal forms also differ.

4.1.1. Porosity and syntaxial cement volume

In both the 2D and the 3D studies, the crystal form $40\bar{4}1$ produces model outputs with a lower porosity than the crystal form $01\bar{1}2$ (Figure 9), as the mean volume of the syntaxial cement developed by the crystal form $01\bar{1}2$ is lower than that of the crystal form $40\bar{4}1$. For the high monocrystalline content samples, the porosity converges to about 17% for the synthetic samples with the crystal form $01\bar{1}2$, and to about 4% for the synthetic samples with the crystal form $40\bar{4}1$. This difference in the porosity in the 3D study (about 13%) stands in contrast to the difference of about 3% in the 2D study, where the porosity of the high monocrystalline content samples converges to about 16% in the case of $01\bar{1}2$ and to about 13% in the case of $40\bar{4}1$.

This 4-fold difference in the porosity of the high monocrystalline samples in the 2D study compared to the 3D study stems essentially from the dimensionality of the two models. In the 3D model, the volume of the syntaxial cement produced is controlled by the *volume* of the bounding polyhedron reduced by the volume of the grain itself. As Figure 1c illustrates, the volume of the epitaxial overgrowth developed in the absence of obstacles on a spherical grain by a rhombohedral form $40\bar{4}1$ is 9.6 times larger than the volume developed by the crystal form $01\bar{1}2$.

In the 2D methodology, however, the amount of the syntaxial cement is controlled by the cross-sectional *area* of a crystal form circumscribed on a monocrystalline grain reduced by the area of the grain itself. The 2D methodology assumes that the grain visible in the plane of the porous medium is cut close to its centroid (see Appendix B). As the crystal axis of a monocrystalline grain can be oriented in any direction, the cross-section of the bounding polyhedron can take a range of shapes and its area will vary accordingly. A comparison between the mean cross-sectional area of the two crystal forms circumscribed on an identical

spherical grain (which is achieved by rotating the rhombohedra by a full range of angles in the 3D) reveals that the mean amount of the syntaxial cement that would be produced in the absence of obstacles in the case of $01\bar{1}2$ is 5.5 times smaller than in the case of $40\bar{4}1$. This ratio is 1.7 times smaller than the ratio of volumes of the syntaxial cement produced on a spherical grain by the two rhombohedral forms in the 3D model (which is 9.6). The difference in the ratios between the 2D and the 3D model is the main reason for the difference in the porosity of the cemented synthetic samples.

It should be noted, however, that in a porous medium syntaxial cement will rarely develop to its full crystal form, due to the effect of the impinging grains. That is why the factor of 9.6 (in the 3D study) does not translate into the difference in the cement volume produced in the 3D cemented synthetic samples. In the absence of the isopachous cement ($\beta = 0$), the volume of the syntaxial cement in the high monocrystalline content samples ($\alpha > 90\%$) is about 21% in the case of $01\bar{1}2$ and about 34% in the case of $40\bar{4}1$. This yields a factor of 1.6, i.e. the crystal form $40\bar{4}1$ produces 1.6 times more cement than the crystal form $01\bar{1}2$. In the 2D study, in the synthetic samples with no isopachous cement, the amount of the syntaxial cement in the high monocrystalline content samples is about 21% in the case of $01\bar{1}2$ and about 24% in the case of $40\bar{4}1$. This yields a factor of 1.1. This is again smaller than the ratio of the mean cross-sectional areas for the two crystal forms (which is 5.5).

In the 3D study, in the absence of isopachous cement, the syntaxial cement in the high monocrystalline content samples in the case of $40\bar{4}1$ obscures 34% of the total sample volume compared to 21% in the case of $01\bar{1}2$. In the 2D study the difference is smaller (2.5%). In both models, this is because elongated crystal form $40\bar{4}1$ can protrude deep into the pore space and often manages to bridge the pore space completely, which crystal form $01\bar{1}2$ achieves much less frequently, as illustrated in Figures 10 and 11.

4.1.2. Mean volume of the isopachous and syntaxial cement per grain

Since the mean volume of the syntaxial cement developed by the crystal form $01\bar{1}2$ is significantly smaller than that in the case of $40\bar{4}1$, the behaviour of the $\beta - \alpha$ curves differs in the two cases in the 3D study. All the curves in the case of $40\bar{4}1$ are decreasing (Figure 12d), which suggests that at any monocrystalline grain content, the mean volume of the syntaxial cement per grain is greater than the mean volume of the isopachous cement per grain. In the case of $01\bar{1}2$, only the curves for the synthetic samples with low width of isopachous cement fringes ($\beta = 0$, 1 and 2 voxels) decrease (Figure 12c). The synthetic samples with $\beta > 2$ produce increasing curves, as the mean volume of the isopachous cement exceeds that of the syntaxial cement as soon as isopachous cement fringes grown to a width of at least 3 voxels ($30\mu m$).

4.1.3. Permeability

In the 3D model results, the permeability at equal porosities of synthetic samples with the crystal form $40\bar{4}1$ is greater than of the synthetic samples with the crystal form $01\bar{1}2$ (Figure 13c and d). This is in contrast to the results of the 2D study and occurs because the monocrystalline grains content in the case of $40\bar{4}1$ in the 3D model has significantly stronger impact on the porosity.

The difference in the porosity of the synthetic samples with an equal content of the monocrystalline grains (α) and equal width of the isopachous cement fringes (β) in the 2D study reaches up to 3% for the high monocrystalline content samples, the difference in the 3D study is about 13%. This is primarily an effect of the shape differences between the two rhombohedral forms of calcite modelled. The crystal form $40\bar{4}1$ generates more elongated features that may reach further in the pore space, so blocking the flow paths. The probability of closing the flow pathways that significantly contribute to the flow is therefore greater, and this is reflected by the permeability being on average lower.

In the 3D modelling, the permeability of synthetic samples of equal porosity is higher in the case of $40\bar{4}1$ than in $01\bar{1}2$ because fewer monocrystalline grains are needed to produce an equal volume of cement. Fewer monocrystalline grains

producing syntaxial cement of the crystal form $40\bar{4}1$ result in a patchy cement fabric in the sample and in a higher permeability, than the more uniform distribution of cement produced by more monocrystalline grains in the case of crystal form$01\bar{1}2$.

When we consider the synthetic samples with no isopachous cement, we observe that slightly *more* monocrystalline grains are necessary to generate a sample of equal porosity in the 3D study than in the 2D study in the case of crystal form $01\bar{1}2$. However, in the case of $40\bar{4}1$, significantly *fewer* monocrystalline grains are necessary in the 3D study (see Figure 9). The fewer monocrystalline grains there are, the less likely it is that they close off pore space and, so reduce permeability.

4.1.4. Variability in the synthetic data

In most results generated, the variability in the results is greater for synthetic samples with the rhombohedral form $40\bar{4}1$. This is explained by the potential volume of cement generated by crystal form $40\bar{4}1$, which is 9.6 greater than crystal form $01\bar{1}2$. The extent to which this volume is realised in the course of the cement growth depends on the proximity of the neighbouring grains, the type of cement that the neighbouring grains develop and the orientation of the crystal axis of the grain in question. The *location* of the neighbouring grains is pre-determined as it is an input to the model in the form of the image of grain deposit, and the cementation model has a limited control on changing the neighbourhood of any given grain, as it can only add cement around the existing grains. However, the *orientation* of the crystal axis of a grain is determined entirely at random in Stage 1 of Calcite2D or Calcite3D. Therefore, it is mainly the orientation of the crystal axis that controls the amount of cement grown by a monocrystalline grain.

This effect is illustrated in Figure 10c, where the elongated form of the syntaxial cement is visible in the top-left corner (coloured light orange). The crystal axis of this grain is oriented vertically in the image, which enables the cement growth into the large pore area above the grain. If the crystal axis was

instead oriented horizontally, the cement growth would soon be blocked by the grains impinging on both sides, resulting in a much smaller volume of cement for that grain. The effect of the impingement by the neighbouring grains on limiting syntaxial cement growth can be observed e.g. for the largest grain in the sample (Figure 10c, centre bottom of image, light orange cement).

The monocrystalline grains that grow according to the crystal form $40\bar{4}1$ have the potential to grow a large volume of cement, but whether this potential is achieved depends on the direction of the crystal axis of the grain. Overall, the crystal form $40\bar{4}1$ can produce a wide range of cement volumes for a single grain. As a result, the variability in the porosity of the cemented synthetic samples is considerable. In contrast, the crystal form $01\bar{1}2$ produces blocky cement shapes, with a much smaller aspect ratio, and the random effect of the orientation of the crystal axes does not have such a great impact on the volume of cement produced.

4.2. Cement volume

The porosity of the synthetic samples is generally lower in the 3D study than in the 2D study, as the volume of cement produced is higher. The cement in the 3D model is grown in all three directions, and often reaches sections of the 3D medium in which the grain that produces this cement is not visible, as illustrated in Figure 8. The cement in the 2D model is seeded only by grains that are visible in the plane of the porous medium, and thus the final cemented medium lacks cement that could grow into that plane by grains that are not visible, and so leading to lower porosities.

4.2.1. Syntaxial cement

This section concerns the synthetic samples where only syntaxial cement is present ($\beta = 0$). Syntaxial cement volume developed by a monocrystalline grain depends on the shape of the grain, its size, the direction of the crystal axes, the proximity and the arrangement of the neighbouring grains, and the shape of the crystal form developed.

Let us consider a single grain of a diameter $250\mu m$ in both versions for the model: the 3D model where the porous medium has dimensions of $3 \times 3 \times 3mm$, and the 2D model where the porous medium has dimensions of $10 \times 10mm$. In the absence of any obstacles, the porosity occlusion by the syntaxial cement of the crystal form $01\bar{1}2$ growing on a spherical grain with diameter $250\mu m$ is 2.3 times greater in the 3D medium than in the 2D medium. An equivalent grain developing syntaxial cement of the crystal form $40\bar{4}1$ would obscure 3.9 times as much porosity in the 3D medium than in the 2D medium. The volume of cement in the 3D model is calculated here as the *volume* of the circumscribed polyhedron reduced by the volume of the grain. The 'volume' in the 2D model is the mean cross-sectional *area* of the bounding polyhedron with a plane passing through the centre of the grain, again reduced by the surface area of the grain.

Although the syntaxial cement volume in the synthetic samples with the crystal form $01\bar{1}2$ is very similar in the 2D and 3D studies (about 21% of the volume of the sample), the factor of 2.3 obtained above suggests that the porosity should be occluded more in the 3D modelling. In the case of $40\bar{4}1$, a significant difference in the cement volume produced is observed: 34% of the sample volume in 3D and 24% in 2D, but the ratio is still significantly smaller than the factor of 3.9 obtained above for a spherical grain in the absence of obstacles.

The reason why the difference in the porosity occlusion between the 3D and 2D models is not as high as the factor 2.3 in the case of $01\bar{1}2$ and the factor 3.9 in $40\bar{4}1$, is primarily due to the effect of the impinging grains. This results in that the full volume of the bounding polyhedron that would develop in the absence of impinging grains cannot realised at this stage of modelling.

An additional factor that curbs the ratio of the porosity occlusion in the 3D and the 2D models is the size of grains in the sample. The volume of the cement produced is controlled by the size of the grain. The mean grain size (equivalent diameter) is slightly smaller in the 3D study ($260\mu m$ compared to $285\mu m$ in the 2D study), which leads to a smaller cement volume per grain produced. Moreover, the grains size distribution in the 2D model is wider and the grains are on average larger than in the 3D medium, leading to a greater

cement volume produced per grain in the 2D study.

Lastly, the difference in the complexity of grain shapes might influence the volume of cement produced by a grain. The grains in the 3D synthetic deposit are very regular and their 2D cross-sections show rounded convex shapes (Appendix C). This is not the case in the 2D porous medium, which includes non-convex grains, often with a convoluted perimeter (Figures **??**. The irregularity of the grain shapes leads to a greater occlusion of the porosity in the 2D model, particularly in the case of the syntaxial cement, as the cement needs to fill in these concave irregularities.

4.2.2. Isopachous cement

In the synthetic samples with no or few monocrystalline grains, increasing the width of the isopachous cement fringes (β) is very effective in decreasing porosity. This effect is even stronger in the 3D model results than in the 2D results: a width of $50\mu m$ in the 3D study (5 voxels) occludes the porosity of the synthetic samples by 31.2%, while the same width of $50\mu m$ in the 2D study (10 voxels) occludes the porosity by 21.2%.

The difference between the 2D and 3D model arises again from the dimensionality of the two models. In the 2D model, all grains develop equal thickness of the isopachous cement fringes. In the 3D model, even though the *true* thickness remains the same for all grains, the *apparent* thickness of the isopachous cement fringes visible in the 2D sections of the 3D medium depends on the distance of the centroid of the grain to the plane of section. The larger this distance is, the larger the apparent thickness of the isopachous cement fringes. As the plane of section is unlikely to cut exactly through the center of the grain, the vast majority of the isopachous cement fringes observed in any given section have thicknesses appearing larger than the input to the cementation model (β). Overall, this leads to seemingly differing thickness of the isopachous cement fringes in 2D sections of any 3D cemented synthetic sample.

The increased volume of the isopachous cement in the 3D study with respect to the 2D study in the case of $01\bar{1}2$, results in the mean isopachous cement vol-

ume produced per a polycrystalline grain being bigger than the mean syntaxial cement volume produced per a monocrystalline grain for $\beta > 20\mu m$. This is reflected in the decreasing curves in Figure 12.

4.3. Competition for pore space

The concave shape of the curves in Figure 12 suggests a competition between the syntaxial and the isopachous cements for growth space. The change of slope in the curves of the porosity as a function of the monocrystalline grains content is an effect of the competition between syntaxial cements for the available pore space (see Sections 1.2). The more monocrystalline grains there are in a sample, i.e. the larger α is, the smaller difference it makes for the final cement volume if more monocrystalline grains are added. This is because a smaller volume of the *potential* syntaxial cement can be actually grown, as there is less pore space available. The competition effect is found in other fields, such as the Langmuir adsorption model, where the molecules are competing for the adsorption sites [42].

The fact that the slopes in Figure 12 are becoming increasingly more linear with the increasing width of the isopachous cement fringes (β), shows that the larger the width of the isopachous cement fringes (and the resulting average amount of the isopachous cement produced per grain), the smaller difference it makes if more monocrystalline grains are added. The thicker the isopachous cement is allowed to grow, the more aggressive competitor for the pore space it becomes for the syntaxial cement. As a result, the competition between the monocrystalline grains developing syntaxial cement has a smaller impact on the overall volume of cement, i.e. the monocrystalline grains have smaller impact in the synthetic samples with more isopachous cement.

4.4. Permeability

Here we examine the permeability results and discuss the effectiveness of the isopachous cement in closing the pore-throats, the variability in the results, and a comparison of the poroperm results derived in our study with data for

grainstones noted in the literature. Finally, the impact of the monocrystalline grains on the permeability is discussed.

4.4.1. Effect of isopachous cement on limiting permeability

The fact that there are no percolating cemented synthetic samples for the isopachous cement fringes width of $\beta = 3$ pixels ($15\mu m$) and higher (e.g. Figure 9) in the 2D study, means that isopachous cement is very effective in closing off the pore-throats. Just a $15\mu m$-thick rim is enough to render a cemented synthetic sample impenetrable, regardless of the content of the monocrystalline grains. For example, a synthetic sample with $\beta = 3$ pixels and *no* monocrystalline grains does not percolate. In contrast, in the 3D study almost all samples are percolating, even those where the width of the isopachous cement fringes reaches $50\mu m$.

In the plots representing the dependence of the permeability on the porosity (Figure 13) and the monocrystalline grain content (Figure 14), the results for the synthetic samples for different values of the width of the isopachous cement fringes (β) are grouped together. In particular, the synthetic samples with $\beta = 2$ pixels in the 2D study form an isolated cluster in the low permeability zone. This clustering suggests that the amount of the isopachous cement is a strong control on the permeability.

This is further illustrated in Figure 15, which shows the velocity of flow for four samples: a back-stripped medium used as an input in Calcite2D and three cemented synthetic samples with no or low monocrystalline grain content and $\beta = 0, 1$ and 2 pixels. Model output b) illustrates that at a low monocrystalline grain content ($\alpha = 12.2\%$), syntaxial cement lowers the permeability by excluding from the flow regions of the pore space by cutting them off with interlocking crystals (areas outlined with a green dashed line). The exclusion of these regions from flow results in a 23% reduction in the permeability compared to the back-stripped medium (a). This is not a dramatic change in the permeability.

However, when a comparable amount of the isopachous cement is introduced around all grains, as in the synthetic sample c), the change in the permeability is

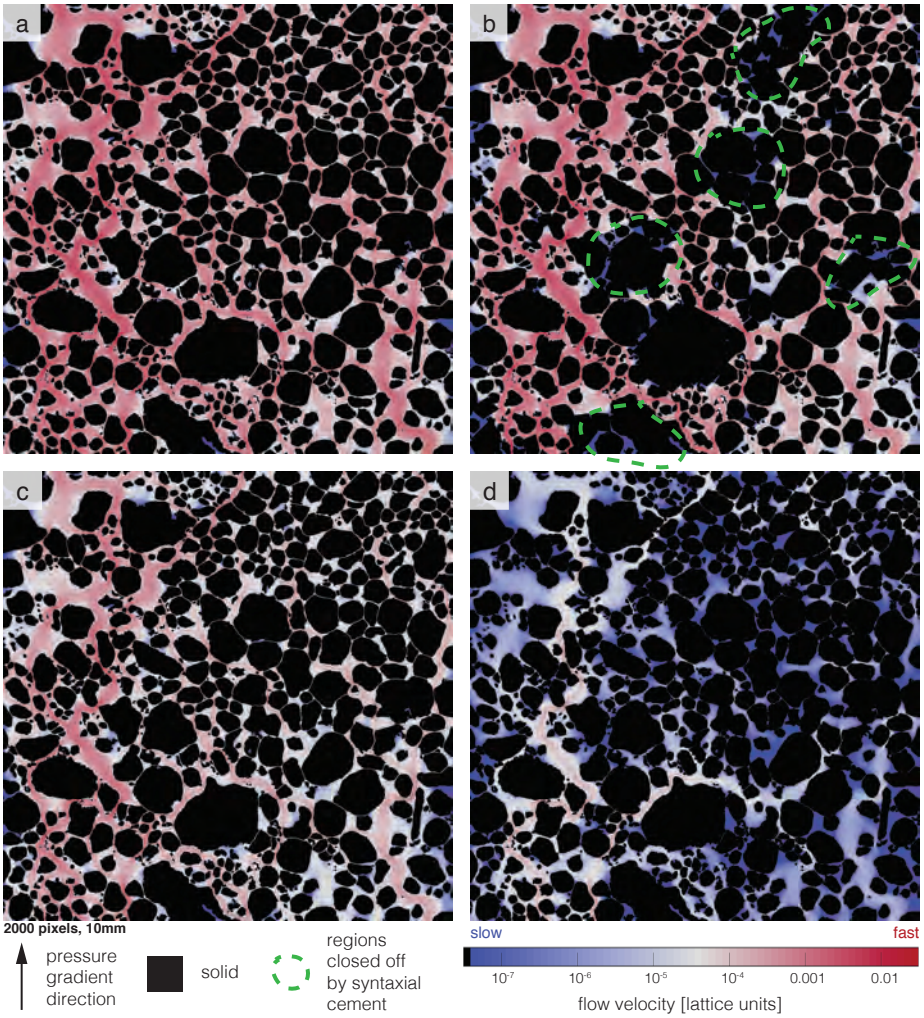

Figure 15: The log of magnitude of the flow velocity for the synthetic samples with none or low monocrystalline cement content and varying width of the isopachous cement fringes: a) the back-stripped sample ($\alpha = 0$, $\beta = 0$, $\phi = 36.3\%$, $\kappa = 7940mD$), b) a synthetic sample with no isopachous cement and a few monocrystalline grains ($\alpha = 12.2\%$, $\beta = 0$, $\phi = 33.5\%$, $\kappa = 6110mD$), c) a synthetic sample with $5\mu m$ width of the isopachous cement fringes and no monocrystalline grains ($\alpha = 0$, $\beta = 1$, $\phi = 33.4\%$, $\kappa = 2420mD$), d) a synthetic sample with $10\mu m$ width of the isopachous cement fringes and no monocrystalline grains ($\alpha = 0$, $\beta = 2$, $\phi = 30.6\%$, $\kappa = 130mD$).

much greater: it is reduced by 70% in comparison to the back-stripped sample a). The isopachous cement fringes with a width of 1 pixel (representing $5\mu m$) have such a strong impact on the permeability because *all* pores are narrowed and thus the velocity of the flow through them decreases considerably. Increasing the width of the isopachous cement fringes even further to 2 pixel ($10\mu m$) in the synthetic sample d) results in a permeability reduction of 98% compared to the back-stripped sample. The majority of the narrow pore throats in the synthetic sample d) are closed off completely and the flow is possible only thanks to the high porosity pathway on the left side of the image.

Figure 16 illustrates flow velocity derived with a LB simulation in two model outputs of Calcite3D. Both synthetic samples consist only of polycrystalline grains. The synthetic deposit with no cement (Figure 16a) has a porosity of 37.8% and a permeability 59,800mD. The introduction of the isopachous cement fringes of width $50\mu m$ (Figure 16b) decreases the porosity to 6.6% and the permeability to $114mD$. Although the isopachous cement fringes occlude the vast majority of the pore space, the flow manages to continue due to the connectivity of pores in all three dimensions, unlike in a 2D medium.

4.4.2. Variability in the synthetic data

The permeability results in the 3D study span four orders of magnitude (Figure 13c and d), but for the synthetic samples with similar porosity, the variability in the permeability does not go beyond $log(\kappa) = 0.54$. The poroperm can be fitted with an exponential curve with a high coefficient of determination (R^2), demonstrating a clear pattern with little variation in the synthetic data. This is in contrast to the 2D study, where the variability at any given porosity spans up to two orders of magnitude, as illustrated in Figure 13a and b. The fact that it is not the case in the 3D study is a result of the removal of the 2D bias in flow simulation. Flow simulated in 2D might lead to a bias in the permeability and skewing of the results towards smaller values, as the 2D media lack the pore connectivity in the 3^{rd} dimension. The clear trend in the poroperm data exhibited in the 3D results confirms this speculation: the pore connectivity

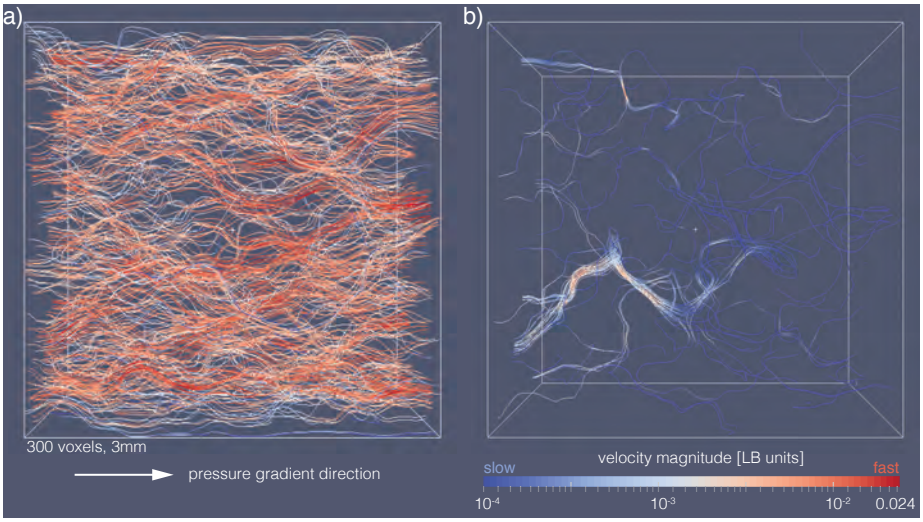

Figure 16: The magnitude of the flow velocity on a logarithmic scale displayed along the streamlines for samples with no monocrystalline grains content and different width of the isopachous cement fringes: a) a sample with no cement ($\alpha = 0$, $\beta = 0$, $\phi = 37.9\%$, $\kappa = 59800mD$, $S = 298mm^2$, $T = 1.22$), b) a sample with $50\mu m$ width of the isopachous cement fringes ($\alpha = 0$, $\beta = 5$, $\phi = 6.6\%$, $\kappa = 100mD$, $S = 114mm^2$, $T = 2.42$).

is maintained in all three dimensions, and so the permeability results exhibit a much narrower range.

Another trend observed in Figure 13a and b is that the variability in the 2D results decreases the more isopachous cement there is in the synthetic sample, i.e. for higher β. This can be explained by the fact that there is less randomness involved in the growth of the isopachous cement, as the only random step associated with the isopachous cement growth in the cementation model is determining whether a grain is to be treated as polycrystalline or monocrystalline. After a grain is labelled polycrystalline in Stage 1 of Calcite2D, isopachous cement grows, pending adjustments due to the impinging grains, to a width determined by the input parameter in Stage 2. In the case of the monocrystalline grains, there is an additional random step of assigning the direction of the crystal axis of the grain, which (together with the arrangement of the neighbouring grains) has a great impact on the volume of the syntaxial cement produced per grain and its impact on flow (see Section 4.1.1).

In other words, the amount of the monocrystalline grains in a sample controls the variability in the permeability: the more monocrystalline grains there are, the larger is the variability in the permeability, as there are more possibilities in the random choice of the placement of the monocrystalline grains in the synthetic sample and in the directions of the crystal growth. Figure 14a and b illustrates this phenomenon, as the three shaded regions for synthetic data associated with the different widths of the isopachous cement fringes (β) increase in width from left (low variability at low monocrystalline grain content) to right (higher variability at high monocrystalline grain content).

The randomness in the location of the monocrystalline grains and the directions of their crystal axes can lead to very different permeabilities in samples of the same porosity,both in 2D (Figure 17) and 3D (Figure 18). All model outputs used to simulate the flow shown in Figures 17 and 18 are generated with the crystal form $40\bar{4}1$ and have no isopachous cement. Both 2D outputs (Figure 17) have porosity of about 27.4%, and the 3D outputs (Figure 18) have porosity very close to 12.3%. The 2D and 3D synthetic samples were selected as two end-points of the synthetic data for $\beta = 0$ and $\phi = 27.4\%$ in 2D and $\phi = 12.3\%$ in 3D in Figures 13b and 13d, respectively: one with the highest and one with the lowest permeability. The parameters that characterise these synthetic samples (the width of the isopachous cement fringes, the monocrystalline grain content, and the porosity) are very similar, but the resulting permeability differs by an order of magnitude in the 2D case (22 times) and by a factor of 3.5 in the 3D case.

This stark contrast in the permeability is directly due to the randomness of the placement of the monocrystalline grains and the directions of the crystal axes. In the high permeability 2D synthetic sample in Figure 17a, there is a high-velocity flow channel in the portion of the sample with higher porosity (left side), which remains open despite cementation and allows a fast flow of fluid though it. Monocrystalline grains are present in that high-velocity channel, but their crystal axes are oriented in such a way that the syntaxial cements do not interlock with other grains, and so do not obstruct the flow. The situation is

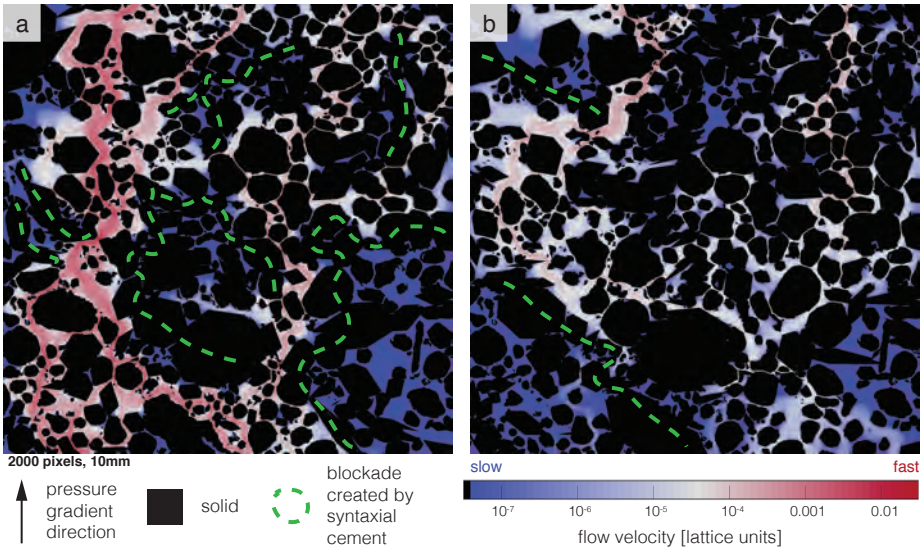

Figure 17: The impact of the randomness in the location of the monocrystalline grains in the synthetic sample and the orientations of their crystal axes on log of the flow velocity. From the group of the synthetic samples with no isopachous cement generated with the crystal form $40\bar{4}1$ and porosity of around 27.4%, two synthetic samples with the greatest difference in the permeability are shown: a) $\alpha = 31.2\%$, $\beta = 0$, $\phi = 27.5\%$, $\kappa = 2450mD$, b) $\alpha = 30.8$, $\beta = 0$, $\phi = 27.4\%$, $\kappa = 110mD$.

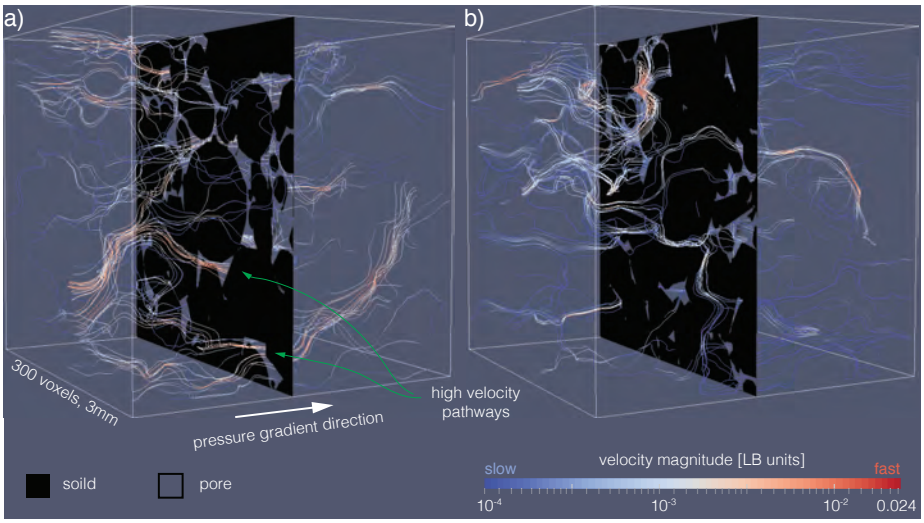

Figure 18: The impact of the randomness in the location of monocrystalline grains in the sample and the orientations of their crystal axes on the flow velocity (displayed along streamlines). From the group of samples with no isopachous cement generated with the crystal form $40\bar{4}1$ and with porosity of around 12.3%, two samples with the largest difference in the permeability were selected: a) $\alpha = 54.4\%$, $\beta = 0$, $\phi = 12.5\%$, $\kappa = 2030mD$, b) $\alpha = 54.9$, $\beta = 0$, $\phi = 12.3\%$, $\kappa = 580mD$.

very different in the low permeability 2D synthetic sample in Figure 17b, where syntaxial cements block off the flow at the top and at the bottom of that high-porosity channel (green lines), and so shut down the main highway for flow in the sample. The flow is therefore forced to continue in a convoluted way, which makes the flow path much more tortuous and significantly lowers the permeability. On the other hand, in the high permeability 3D synthetic sample (Figure 18a) there are multiple high-velocity flow pathways present because the large grain visible in the middle of the cross-section is polycrystalline and so has not developed any cement. In the low permeability 3D synthetic sample (Figure 18b), this central grain has developed syntaxial cement, and as a result it blocked pathways through the middle of the porous medium. This in turn resulted in the majority of the flow concentrating in the top portion of the synthetic sample.

Another factor that contributes towards the wide range of permeabilities for the synthetic samples at similar porosities is the dimensionality of the methodology. As discussed in Section 4.6, the synthetic samples that are percolating in 3D can have non-percolating 2D cross-sections. It is possible that the non-percolating 2D cemented synthetic samples in this study would be found percolating, if 3D pore connectivity was allowed. Similarly, some of the low permeability synthetic samples (e.g. the samples for $\beta = 2$) could have much greater permeability in 3D. The wide range of permeability might therefore be an artefact of the 2D methodology.

4.4.3. Data from the published studies and the plug data

There is no experimental dataset containing the porosity and the permeability data for natural samples with varying content of the monocrystalline grains in grainstones, which would be most useful in validating the results of this study. What does exist, however, are a few datasets of the porosity and the permeability for grainstones. Figure 19 compiles the synthetic poroperm data for cemented samples generated in this study in the context of the published data for natural grainstones, as well as the plug data for several natural samples

of the same rock type as is used as an input porous medium in this study (see Section 2.1.1).

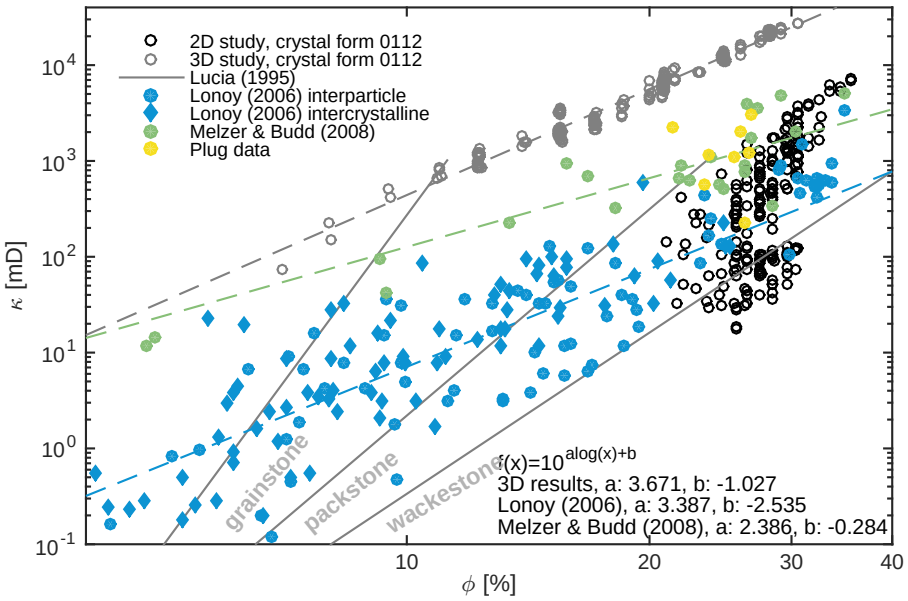

Figure 19: The synthetic poroperm data for the 2D (black) and 3D (grey) model outputs generated with the crystal form $01\bar{1}2$ and data obtained from literature: the divisions from the rock type classification by Lucia [43] (grey lines), the macroporosity data from Løn øy [25] (blue) both for the interparticle (circles) and the intercrystalline porosity (diamonds), the data for grainstones from Melzer and Budd [44] (green circles) and the plug data derived for the same rock type as is used as the input in the study (yellow circles).

None of the synthetic samples with a porosity less than 20% generated in the 2D study are percolating and so the flow through them cannot be simulated. As a result, all of the permeability results from the 2D study are constrained to a relatively narrow porosity range of the poroperm plot, unlike any of the published poroperm data for grainstones. Moreover, the wide range of the permeability results for the available porosities might be an artefact resulting from the 2D methodology (see Section 4.6), as mentioned in the previous section. This should be taken into account when comparing poroperm results from this study with experimental data.

Recall that the cementation model is based on an initial porous medium which is derived through the segmentation of a thin-section image followed by

two post-processing steps: firstly the separation of grains and then the removal of the fine grains. The post-processing steps have a negligible effect on the porosity of the sample, but the effect on the permeability can reach up to 12% (see Section 2.1.1). As a result, the permeability of the cemented samples generated in this study might be higher than if they were generated using the pre-processed image. The separation of grains affects the permeabilities of the samples with no isopachous cement the most, and so the permeability of these samples might be overestimated the most. The effect of the separation of grains is canceled by the growth of the isopachous cement, so the permeability of the samples with isopachous cement fringes is probably not significantly different than it would be if the pre-processed medium was used. Overall, if the pre-processed medium was used, the samples with $\beta = 0$ would have a permeability lower by up to 12%, while the permeability of the samples with $\beta = 2$ would not change by much. This would shift the high-permeability samples down in the poroperm plot so that the range of permeabilities exhibited by all cemented synthetic samples would be smaller.

The classification by Lucia [43] places the synthetic samples generated in the study in the packstone sector of the poroperm (Figure 19), as the permeability is too low to place it in the grainstone sector. Note, however, that the permeability results obtained in this study might be artificially low due to the modelling of flow in the 2D, which might be causing the shift of the results down on the poroperm plot, towards the packstone sector. Also, the permeability of the syntaxial samples with no isopachous cement ($\beta = 0$) might be overestimated due to the use of the post-processed image of the porous medium. The interparticle and the intercrystalline macroporosity data by Løn øy [25] have a decent overlap with the synthetic data from this study, albeit the results in this study show more variability in the permeability. Some of the natural samples of the cement-dominated grainstones analysed by Melzer and Budd [44] fall within the poroperm range as the synthetic samples generated in this study, particularly in the higher permeability portion. The same happens in the case of the plug data associated with the rock used in this study. In summary it can be concluded

that Calcite2D produces synthetic samples with porosities and permeabilities that are more or less realistic for carbonates.

The permeability of the synthetic deposit, generated in the 3D study with the use of the deposition model, is 59,800mD at porosity 37.9%. This is just above the maximum (56,600mD) reported for Holocene grainstone sediment permeabilities as reported by Enos and Sawatsky [45]. However, the highest permeability grainstone samples in their study have porosities higher than the one used in this study (45.2-48.2%). For samples in the porosity range 40.1-42.0%, which is closer to the porosity of the synthetic deposit in this study, permeabilities in the range 24,900-31,900mD are reported. This is significantly lower than the permeability of the synthetic deposit produced by the depositional model used in this study.

This high permeability could be attributed to the approach taken to model the shapes of grains and the fact that these are rounded and convex. The ellipsoidal grains in the deposition model developed in this study have only few points of contact with the neighbouring grains, so that the narrowest portions of pore throats are effectively very short (Appendix C). The model thus results in the creation of relatively large interstitial spaces, which allow for unobstructed fluid flow. The effect of pore spaces being too large, and grains touching only at few points of contact, is also due to the 3D modelling methodology not taking the mechanical compaction into account. In natural porous media, grains fit much closer together and narrow pore throats are common (Figure 3a), leading to constriction of fluid flow and, as such, lower permeabilities.

Another reason for the increased permeability of the synthetic deposit in the 3D model may be the choice that is made in the treatment of the porous medium to remove the fine grains (Section 2.1.1). The absence of fine grains is propagated from the 2D to the deposition model in the 3D (Appendix C). As the statistics of grain shape and size are an input to the grain generation model, the removal of fine grains results in very fine grains being absent from the 3D deposition model. In addition, the pores and pore throats in the synthetic 3D deposit are unnaturally wide due to the perfect convexity and regularity of the

grain shapes (as discussed above). This allows fine grains that are generated in the deposition model to fall freely through the wide pores to the bottom of the deposit, which is then cropped to avoid artefacts (Appendix D). The result is that the finest grains are altogether removed from the synthetic sample. Figure 7 illustrates that a good number of fine grains are present in the 2D medium (on the left border of the image in Fig 7a) and the number of such small grains is significantly reduced in the 3D medium (Fig 7b). The absence of fine grains in the synthetic 3D deposit impacts its permeability by rendering the wide pores and pore throats even less obstructed for fluid flow. Their absence also reduces the potential seeding sites for cement, resulting in higher permeability of the cemented model outputs.

As the permeability of the synthetic *deposit* is so high, the permeabilities of the *cemented* synthetic samples are higher than values reported for the natural carbonates and also higher than the samples of the same rock type as is used in this study to generate the synthetic deposit (Figure 19). Eight reservoir samples of the same rock type as the sample used in modelling (Figure 19) have a mean porosity of 24.9% and a mean permeability of $1450mD$, while this study predicts a permeability of 13,000mD at this porosity.

Another reason for the mismatch between the permeability of the cemented model outputs and the plug data is the difference in scale of the samples. The synthetic samples in the 3D modelling are $3mm^3$, while the other data presented in Figure 19 are plug data derived for cm-scale samples (typically with a diameter of around $4cm$). There is an order of magnitude difference in these scales and, naturally, the larger scale samples have a potential of being more heterogenous. The synthetic samples generated here model a single highly permeable rock type. It is not inconceivable that some mm-scale sub-samples of the plugs presented in Figure 19 are equally highly permeable and the fact that their permeability is much lower compared to model outputs is caused by the presence of less permeable layers in the plug. The plug samples therefore capture more of the heterogeneity of the rock, including the less permeable layers, and this is one of the reasons why the cementation model over-predicts the permeability of

the plug data.

Upon the investigation of the *trend* in the poroperm results of the synthetic samples produced in this study, it can be concluded that their behaviour is very similar to that of natural carbonate grainstones. The slope of the exponential fit to the interparticle and intercrystalline macroporosity data by Lønøy [25] (blue line in Figure 19) is strikingly similar to the fit to the synthetic samples in the 3D study (dashed grey line). The slope differs somewhat from the fit to the poroperm data for the cement-dominated grainstones analysed by Melzer and Budd [44] (green line) but the classification by Lucia [43] (grey lines) places the synthetic samples from this study in the grainstone sector of the poroperm.

It can be concluded that Calcite3D produces samples with permeabilities higher than in the typical natural media, which can be attributed mainly to the deficiencies of the *deposition* modelling methodology, which produced a synthetic deposit with unnaturally wide pores. However, the response of the synthetic deposit to cementation, which produces a similar poroperm trend as observed in the natural media, suggests that the *cementation* methodology is successful in modelling realistic *changes* in the cement volumes and in the pore space morphology.

4.4.4. Dependence on the sediment type

One goal of this study is to investigate the impact of early calcite cement growth on the evolution of permeability. This was achieved by changing the content of the monocrystalline grains. The 2D study suggests a strong dependence, as illustrated by the steep slope of the contours in Figure 14a and b. However, the steepness of slopes is a result of a significant variability in the permeability for the synthetic samples of equal porosity, which in turn is an effect of the flow modelling in 2D.

In the 3D study, in the case of the crystal form $01\bar{1}2$, the dependence of the permeability on the monocrystalline grain content is subtle but clear (Figure 14c). In the case of $40\bar{4}1$ the contours are close to horizontal (Figure 14d), thus the dependence of the permeability on the monocrystalline grains content

remains inconclusive.

Overall, the results of this study suggest that the composition of a carbonate deposit, i.e. the amount of the monocrystalline and polycrystalline grains in the sample, is a *weak* control on the final permeability of the sample under the early calcite cementation regimes investigated. Indeed, we show rather that the nature of the dependence of the permeability on the content of monocrystalline grains in a sample is controlled by the crystal form developed by syntaxial cement.

4.5. Model limitations

Implementation of cementation continues in pores even after they are cut off from the percolating pore space by growing cement. This limitation is somewhat mitigated by the fact that in realistic scenarios complete separation of pores rarely happens as there is usually a *micro-scale* connection to the percolating pore space. As the resolution of the models presented in this study is quite coarse ($5\mu m$ in the 2D study) micropores or pore throats are sub-resolution. Moreover, in the case of the 2D model, the pores that are rendered disconnected in 2D would almost always would have connectivity with percolating pore space through the 3^{rd} dimension.

4.6. Deficiencies of the 2D methodology

One of the caveats of the modelling methodology is that it requires two steps of manual intervention to the binarised porous medium: 1) introduction of thin pore throats to separate touching grains and 2) removal of very fine grains. Both these interventions, however, result in a negligible increase of the porosity of the medium, as it is increased by a mere 0.17% from 36.14% to 36.31%. The effect of these interventions on permeability is larger, as it is increased by $860mD$ from $7080mD$ to $7940mD$ (12.1% change), but it is still relatively minor.

In an effort to introduce a full flexibility in the directionality of the c-axes of monocrystalline grains in 3D, Stage 1 of Calcite3D involves a creation of a surrogate 3D grain, as noted in Appendix D. For that purpose a distance between the 2D centroid and the 3D centroid is modelled with a normal distribution

that takes into account the size of the grain. This choice is somewhat arbitrary and it can be argued that other distributions would perform better in creating a realistic porous medium (e.g. a uniform distribution).

In a 3D deposit, growing cement expands in all three dimensions. As a result, a 2D cross-section of a naturally cemented 3D sample will often exhibit cements grown by grains that lie outside of the plane of that section, i.e. the cement is present in the section but the grain is not. In the 2D cement model presented in this study, cement is only grown on the grains present in the initial porous medium. The possibility of other grains growing cement into the plane of the medium is not taken into account. This is another limitation inherent to the 2D model set-up.

Lastly, the most notorious limitation of the 2D rock modelling in terms of its usability in permeability prediction is the fact that the pore connectivity in the 3^{rd} dimension is lost. This leads to unrealistically low permeability predictions. For instance, the experimental permeability associated with the rock used in this study is $\kappa = 4700mD$, while the segmented and binarised 2D image of the same porous medium is not percolating (see Section 2.1.1). This stark difference in permeability highlights the limitation of modelling permeability in the 2D. The fact that there is no pore connectivity in a 2D cross-section of a 3D medium does not mean that there would be no connectivity in the equivalent 3D medium.

Another contribution to the difference in permeability between experimental data and the thin-section image comes from the heterogeneity of the rock. The fact that a sample of a given rock has a high permeability does not mean that another sample of the same rock must have the same, or even similar, permeability.

4.7. Comparison of 2D with 3D methodology

The deficiencies inherent to the dimensionality of the 2D methodology, as discussed in Section 4.6, are eliminated in the 3D methodology. Modelling of the distance between the surrogate 3D grain and the 2D grain is not an issue as in the 3D methodology the *actual* 3D grains are used to find the bounding

polyhedron. The cement grows in all three dimensions, and so certain sections of a cemented 3D porous medium exhibit cement associated with a grain that is not present in that section (Figure 8b). Modelling in 3D means that the connectivity of pores is maintained in all three dimensions, so there is no bias in the permeability modelling resulting from the lack of connectivity in the 3^{rd} dimension.

One aspect where the comparison of the two methodologies reflects unfavorably on the 3D model is the resolution and the sample size that can be achieved. Voxel size in the 3D study is twice as big as the pixel size in the 2D study ($10\mu m$ vs $5\mu m$). Sample size in the 3D study is 0.3 the sample in the 2D study (3mm vs 10mm, respectively). The number of grains modelled, however, is almost 150% the number of grains considered in the 2D study (604 and 893 grains, respectively). So, even though the sample is smaller, a larger representation of grains is considered in the 3D model.

4.8. Deficiencies of the grain deposition model in 3D

One step in the 3D methodology identified as a potential source of inaccuracies in the modelling is the methodology to create a 3D synthetic deposit based on statistics describing the size and shape distribution of grains observed in a 2D thin-section image (Section 2.2.1). While this method is successful in generating deposit with very similar *porosity* and *grain size* distribution to those observed in the 2D thin-section, the distribution of the grain *shapes* differs considerably. The current 3D method produces grains that are on average considerably more rounded than those observed in the 2D thin-section image (see Appendix C).

The mismatch in grain shapes might arise from the way in which 2D statistics are used to define the shape of the 3D grain. The 3D grains are created in the form of ellipsoids with one major axis and the other two axes equal, so that the ratio of the length of the minor and the major axes is equal to the shape parameter (the eccentricity). All of the cross-sections in the direction parallel to the longest axis of such an ellipsoidal grain are circular. Since it is the longest axis of the grain, the number of cross-sections in a voxelised medium is also the

largest in that direction. As a result, grain cross-sections that can be visible in a section of a 3D porous medium are more likely to be close to circular.

To address this issue several steps may be undertaken:

1. The shape and the size parameters derived from the 2D thin-section may be used in some other way, e.g. by applying the shape parameter as a ratio of the length of the major and a minor axis of the ellipsoid and modelling the length of the third axis in some other way.
2. The library of shapes available can be extended to introduce more convex shapes, e.g. cylinders or cones, and perhaps even non-convex shapes.
3. Other variables describing the grains visible in the 2D thin-section can be explored, e.g. the equivalent diameter that is used as present as the size parameter could be substituted with the length of the major axis of the grain.

5. Conclusions

The work presented here examines early calcite cementation on the evolution of porosity and permeability. For that purpose a 2D and a 3D model is developed which implements syntaxial cement growth on the monocrystalline grains and isopachous cement growth on the polycrystalline grains. This model is used to generate cemented samples based on a real rock deposit following the methodology detailed in Section 2. Model outputs are generated for two common crystal forms of calcite. The generated synthetic samples are analysed with respect to several quantities of interest: the monocrystalline grain content, porosity and permeability.

The results demonstrate the effect of the competition of growing grains for the available pore space: the more monocrystalline grains there are in the sample, the stronger the competition is and the smaller the impact of each individual grain on the resulting early calcite cement volume or porosity.

Concerning the model outputs produced using different crystal forms of calcite, the differences in the volume of the syntaxial cement and the porosity,

arising from the difference in the shapes and volumes of the two crystal forms, are more pronounced in the 3D model results than in the 2D results. In the 3D model, the cements are 3-dimensional and their growth is not restricted to sections of the 3D medium where the grain seeding the cement is present.

The synthetic samples with syntaxial cements grown according to the more elongated crystal form $40\bar{4}1$ have porosity lower compared to the samples grown according to the more blocky crystal form $01\bar{1}2$ at the same monocrystalline grains content. Moreover, in the 2D the permeability at constant porosity is smaller for the synthetic samples with the form $40\bar{4}1$ but in 3D the permeability at constant porosity is also higher for the synthetic samples with the crystal form $40\bar{4}1$. Additionally, samples with the crystal form $40\bar{4}1$ exhibit greater variability in the results because this rhombohedral form is more elongated and has a greater potential for producing larger volume of cement.

The variability in the results stems from randomness in the location of the monocrystalline grains and the directions of their crystal axes. Contrary to polycrystalline grains, the methodology for monocrystalline grains dictates an additional random step of assigning the direction of the crystal axis of the grain, which (together with the arrangement of the neighbouring grains) has a great impact on the volume of the syntaxial cement produced per grain and its impact on flow. As a result, it can lead to very different permeabilities in samples of the same porosity in both the 2D and 3D results.

The dependence of the permeability on the monocrystalline grains content under the early calcite cementation regimes investigated in this study is found weaker in 3D than in 2D. This may be attributed to the deficiencies of the 2D modelling methodology. The permeability results for some synthetic samples (particularly the low permeability ones) in the 2D study may be artificially low due to the modelling of the flow in the 2D. Additionally, the permeability of the synthetic samples with no isopachous cement or very thin isopachous cement fringes (which are typically high permeability) may be overestimated due to the fact that a post-processed porous medium with artificially separated grains is used. Both of these deficiencies lead to a higher range of permeabilities at

any given porosity in the 2D modelling, and can lead to the dependence of the permeability on the sediment type being exaggerated.

The 3D poroperm can be fitted with an exponential curve with a high coefficient of determination (R^2), demonstrating a clear pattern with little variation in the synthetic data. This is because the pore connectivity is maintained in all three dimensions, and so the permeability results exhibit a narrow range. This is in contrast to the 2D study, where the variability at any given porosity spans up to two orders of magnitude. Moreover, the synthetic samples with $\beta = 2$ pixels in the 2D study form an isolated cluster in the low permeability zone. This clustering suggests that the amount of the isopachous cement is a strong control on the permeability.

The poroperm results of the 2D modelling ($10 - 8000mD$) are in a reasonable agreement with the data reported for grainstones in the literature ($0.1 - 5000mD$) as well as for the plug data of the samples used in the modelling (porosity $22 - 27\%$, permeability $200 - 3000mD$), however the permeability results at any given porosity have a wide range due to the bias inherent to the 2D flow modelling and to the fact that a post-processed medium with separated grains was used in as a basis for the cement growth. The poroperm results in the 3D modelling ($10 - 30,000mD$) exhibit permeabilities above the range of these reported in the literature ($0.1 - 5000mD$) or the plug data of the samples used in modelling (porosity $22 - 27\%$, permeability $200 - 3000mD$), but the reason for that is the initial synthetic deposit, which has a very high permeability ($58,900mD$). However, the *trend* in the poroperm results closely resembles those reported in natural carbonate rocks.

The advantage of working in the 2D is the higher resolution that can be afforded and the significantly lower computational cost. Simulating permeability in 2D, however, has limitations (see Section 4.6) and as a result of these limitations, the permeability results for some synthetic samples might be incorrect.

Regarding the 3D model, we conclude that although the *cementation* methodology is successful in modelling realistic changes in the cement volumes and in the pore space morphology, as the response of the synthetic deposit to cemen-

tation produces a similar poroperm trend as observed in the natural media, the *depositional* methodology is less successful in generating a synthetic deposit with realistic permeabilities. This will be addressed in further work, which will involve expanding the shape library used by the model to introduce less regular grain shapes. A methodology will be developed to optimise the parameters of the depositional model so that the 2D sections of the 3D medium more closely resemble the characteristics of the 2D thin section images of the natural porous media.

Acknowledgements

We are grateful to Petrobras and BG Group for financial support of the International Centre for Carbonate Reservoirs (ICCR). We acknowledge computational time from the UK National Supercomputing Service Archer, under project numbers e417 and d83.

Appendix A. Details of the Treatment of the 2D Porous Medium

Appendix A.1. Automatic segmentation

Since Calcite2D requires a binary image of carbonate *sediment*, the preparation of a thin-section must include segmentation that differentiates between grain, cement and pore as well as binarisation. Automatic methods for image segmentation did not work well for these purposes and significant amount of manual processing was necessary. This is because automatic methods do not differentiate well between grain and cement, which have very similar colour in the original image (Figure 3a). Cement tends to be slightly lighter than the rim of the grain, however the same colour can be found in the grain interior or in other grains located elsewhere in the image. It is therefore impossible to specify a colour filter to target *exclusively* cement without also targeting a significant amount of grain pixels.

The first-pass automatic segmentation that is undertaken here results in the segmentation of the original image (Figure 3a) into two classes that are essentially 'pores' and 'solids'. This segmentation is performed in Matlab on the original image, which has three colour channels: red, green and blue (RGB) and is based on filtering these three colour channels. The 'pore' class is observed to be either blue (high values of the blue channel) or white (high values of all channels), while the 'solids' class has much lower values of the blue channel and significantly higher values of the green and red channels.

Appendix A.2. Manual segmentation

After the initial automatic segmentation differentiating between the pores and solids in the original RGB image is performed, a significant amount of manual adjustment in a graphics package is undertaken to strip the cement off the grains. The resolution of the original colour image (Figure 3a) is 3779 pixels per $1cm$ ($2.65\mu m$) and manual segmentation is performed at that resolution. The resulting sediment image has 775 grains and both convex and concave grains are present.

Appendix A.3. Image resizing

Before the back-stripped binary image undergoes the two post-processing steps the image is resized to a more computationally manageable size of 2000 pixels per $1cm$. This is a good compromise between the resolution ($5\mu m$ is sufficient for the type of modelling in this thesis) and sample size that can be afforded computationally. Resizing results in a negligible change in porosity: the porosity of the 3779^2 pixel image is 36.15% and the porosity of the 2000^2 pixel image is 36.14%.

Appendix A.4. Grain separation

As the cementation methodology requires that all grains in the initial porous medium are disconnected, a manual intervention is required in a post-processing of the back-stripped binary image. In the few instances that two grains are touching, a thin pore-throat is manually added to separate them. Such complete separation of grains is artificial as it does not occur in natural media, especially for those that underwent compaction. Shortly after deposition the grains in grainstone have just a few points of contact in 3D, which in a 2D section manifests as nearly all grains appearing to be disconnected and not touching. However, in the process of compaction the areas of contact between the grains increase, as the grains are pushed against each other. That is why some of the grains are observed to be touching in the thin-section image. However, due to the fact that the number of grain separations required is small, this artificial manual intervention has a negligible impact on porosity: an increase by 0.13% from 36.14% to 36.27%. The impact of grain separation on permeability is larger, but not dramatic: an increase by $640mD$ from $7080mD$ to $7720mD$ (9.0% change, see Table A.2).

This post-processing step impacts the porosity and permeability results of the cemented model outputs. It may artificially increase the porosity of the model outputs by up to 0.13% and the permeability by up to 9%. However, this is an issue mostly for the cemented model outputs with very little cement, as cement growth is very effective in closing the pore throats and making up for

the material that was removed in this post-processing step. This is especially true for the isopachous cement, which renders the all samples non-percolating after only three iterations, which is equivalent to cement fringe 3 pixels or $15\mu m$ thick.

Table A.2: Changes to the properties of the porous medium due to post-processing procedures.

Processing stage of the binary image	Porosity [%]	Permeability (LB) [mD]
back-stripped image	36.14	7080
step 1: grains separated	36.27	7720
step 2: fine grains removed	36.31	7940

Appendix A.5. Fine grains removal

As a further post-processing step, the connected solid pixels with an area smaller than 26 pixels ($650\mu m^2$) are removed from the image (the solid pixels are replaced with pore pixels). These fine 'grains' are mostly artefacts of the automatic segmentation and partly of the manual segmentation procedures and as such are not 'real' grains and a choice is made not to include them in the set of grains of the sample. There are 171 such 'grains' and their removal causes a reduction of the number of grains by 22% from 775 to 604 grains. These very fine 'grains' have a negligible effect on the porosity of the medium as after their removal it is increased merely by 0.04% from 36.27% to 36.31%. Permeability is increased by $220mD$ from $7720mD$ to $7940mD$ (2.8% change, see Table A.2). The fine 'grain' removal makes the subsequent steps in the methodology (Calcite2D stages 1 and 2) less computationally expensive, as the run time of simulations scales with the number of grains. Moreover, the volume of syntaxial cement that would develop on such fine grains would be close to none, rendering the inclusion of these fine 'grains' in cement modelling moot.

Overall, this post-processing step impacts the porosity and permeability results of the cemented model outputs only slightly: the effect on porosity is negligible and the permeability may be artificially increased by up to 2.8%.

Moreover, the fact that these fine 'grains' are mostly artefacts of the segmentation procedures justifies their removal from the image.

Appendix B. Details of the Implementation of Calcite2D

Appendix B.1. Stage 1: grain labelling and crystal axes definition

Appendix B.1.1. Grain properties

After the input porous medium is read, the grains are detected and a structure is created with the properties of each grain: the area in pixels, the position of the centroid, the convex hull area, the list of pixels belonging to the grain, and grain perimeter length. Another property calculated is the list of pixels on the outline of the grain (solid pixels 4-connected to at least one pore pixel).

Appendix B.1.2. Grain labelling

After the allocation of grain properties, grains are labelled as either monocrystalline or polycrystalline based on a random number generator that uses model input parameter α_0; the post-labelling ratio or monocrystalline to all grains α_n will differ slightly from that input. The grain type property is added to the grain structure when the labelling is completed and grain properties are used to calculate the ratio of the 'volume' (actually area) of monocrystalline grains in pixels to all grains α_v as well as the ratio of 'surface area' (actually perimeter length) of monocrystalline grains to all grains α_a.

Appendix B.1.3. Bounds of epitaxial cement

Once the monocrystalline grains are labelled, the bounding polygon that will be filled with cement must be determined. In the case of epitaxial growth, the cement is seeded on non-euhedral faces of the grain in optical continuity to the grain until all faces become euhedral. Due to the fact that calcite belongs to a hexagonal crystal system and the inherent crystal form of calcite is rhombohedral, the shape produced in this rapid growth on non-euhedral faces is a parallelepiped. A parallelepiped, just like a rhombohedron, consists of three

pairs of parallel faces. While all faces of a rhombohedron are rhombs, the faces of a parallelepiped are parallelograms.

The reason for this implementation stems from calcite kinetics. Once a euhedral facet with the same orientation as the calcite rhombohedron is reached during the process of precipitation, epitaxial growth ceases [20]. As a result, only the region within a parallelepiped with three pairs of parallel faces, each of which is tangent to the grain, is created via the very rapid epitaxial growth. After the full shape of the epitaxial overgrowth is reached, mantle growth initiates at a much lower growth rate [20, 9]. Figure B.20 demonstrates the resulting difference in volume between the full rhombohedral form (or rhomb in 2D) and the form that grows epitaxially in the shape of a parallelepiped (or a parallelogram in 2D).

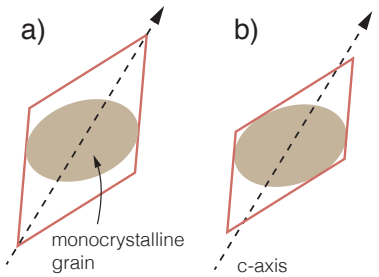

Figure B.20: The difference in the volume between the full crystal form (a) and the form of the syntaxial cement that is developed around a grain in the epitaxial phase, as a result of a rapid growth on the non-euhedral faces (b).

Since the this is a 2D model, the bounding crystals are not in the form of 3D parallelepipeds, but in the form of 2D polygons that can take any possible shape of a *section* of a parallelepiped: a triangle, a tetragon, a pentagon or a hexagon. The approach to finding the shape of this bounding polygon is through a brief venture into the 3^{rd} dimension. For that purpose, a surrogate 3D grain is defined based on the 2D section of the grain as seen in the porous medium image. The smallest parallelepiped that can be circumscribed on this surrogate grain is found and the intersection of that parallelepiped with the plane of the image is determined.

Appendix B.1.4. Plane orientations of the chosen rhombohedral form

Two common rhombohedral forms of calcite are selected for modelling: $01\bar{1}2$ and $40\bar{4}1$ (see Section 1.2.2). The details of the implementation are presented on the example of the rhombohedral crystal form with Miller-Bravais index $01\bar{1}2$.

In the hexagonal system a plane has four Miller-Bravais indices $(hkil)$ which come from intersection of the plane with axes x, y, u and z. Axis u is coplanar with axes x and y and at 60° to both of them [21]. The plane with index $01\bar{1}2$ is parallel to the x-axis ($h = 0$), crosses y-axis at $y = b$ ($k = 1$) and z-axis at $z = \frac{1}{2} \cdot c$ ($l = 2$) (Figure B.21). The following formula can be used to find the vector normal to this plane [21]:

$$n = h\vec{a*} + k\vec{b*} + l\vec{c*} \tag{B.1}$$

where h, k and l are Miller-Bravais indices of the plane and

$$\vec{a*} = \frac{\vec{b} \times \vec{c}}{\vec{a} \cdot [\vec{b} \times \vec{c}]}, \vec{b*} = \frac{\vec{c} \times \vec{a}}{\vec{b} \cdot [\vec{c} \times \vec{a}]}, \vec{c*} = \frac{\vec{a} \times \vec{b}}{\vec{c} \cdot [\vec{a} \times \vec{b}]} \tag{B.2}$$

where $\vec{a}$, $\vec{b}$ and $\vec{c}$ are the vectors defining the unit cell.

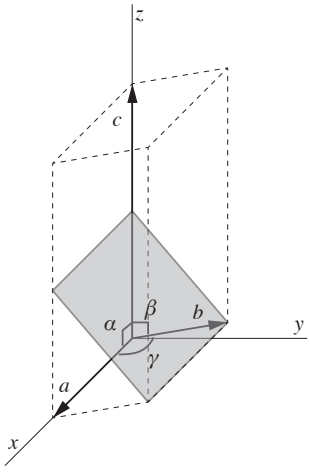

Figure B.21: The unit cell of calcite with the $01\bar{1}2$ plane (shaded), $a = b = 4.991$, $c = 17.062$, $\alpha = \beta = 90°$, $\gamma = 120°$.

The vector normal to the plane with index $01\bar{1}2$ is found using $\vec{a} = \vec{b} = (4.991, 0, 0)$ and $\vec{c} = (0, 0, 17.062)$. The result is $\vec{n_1} = (0, 0.2314, 0.1172)$. Due to the 3-fold rotational symmetry of the hexagonal system about the z-axis the orientations of the remaining planes of the rhombohedral form can be determined by rotating the known plane by 120° and 240° degrees about the z-axis. For that purpose, the Rodrigues' rotation formula can be used:

$$\vec{v_{rot}} = \vec{v}cos\theta + (\vec{k} \times \vec{v})sin\theta + \vec{k}(\vec{k} \cdot \vec{v})(1 - cos\theta) \tag{B.3}$$

where $\vec{v}$ is the vector to be rotated, $\vec{k}$ is the unit vector in the direction or the axis of rotation (in this case $\vec{k} = (0, 0, 1)$) and θ is the angle of rotation. Rotating $\vec{n_1}$ by 120° around the z-axis yields $\vec{n_2} = (-0.2004, -0.1157, 0.1172)$ and rotating by 240° yields $\vec{n_3} = (0.2004, -0.1157, 0.1172)$. A rhombohedron consists of three pairs of parallel faces, so these three vectors ($\vec{n_1}$, $\vec{n_2}$ and $\vec{n_3}$) are sufficient to describe the orientations of all the faces of the rhombohedron.

The three vectors $\vec{n_1} = (0, 0.2314, 0.1172)$, $\vec{n_2} = (-0.2004, -0.1157, 0.1172)$ and $\vec{n_3} = (0.2004, -0.1157, 0.1172)$ describe the angular relationships in the $01\bar{1}2$ rhombohedral form in the case where the crystal axis is parallel to the z-axis. In order to randomise the orientations of the crystals in the sample, all three vectors must be rotated by random angles about the x, y and z axes: θ_x, θ_y and θ_z. This can be achieved with the use of he rotation matrices:

$$R_x = \begin{pmatrix} 1 & 0 & 0 \\ 0 & cos\theta_x & -sin\theta_x \\ 0 & sin\theta_x & cos\theta_x \end{pmatrix}, R_y = \begin{pmatrix} cos\theta_y & 0 & sin\theta_y \\ 0 & 1 & 0 \\ -sin\theta_y & 0 & cos\theta_y \end{pmatrix}, R_z = \begin{pmatrix} cos\theta_z & -sin\theta_z & 0 \\ sin\theta_z & cos\theta_z & 0 \\ 0 & 0 & 1 \end{pmatrix} \tag{B.4}$$

according to the formula:

$$\vec{n_{rot}} = R_x R_y R_z \vec{n} \tag{B.5}$$

where $\vec{n}$ is the vector to be rotated and $\vec{n_{rot}}$ is the rotated vector.

Appendix B.1.5. Surrogate 3D grain

The remaining steps leading to the determination of the 2D bounding polygon are presented in Figure B.22.

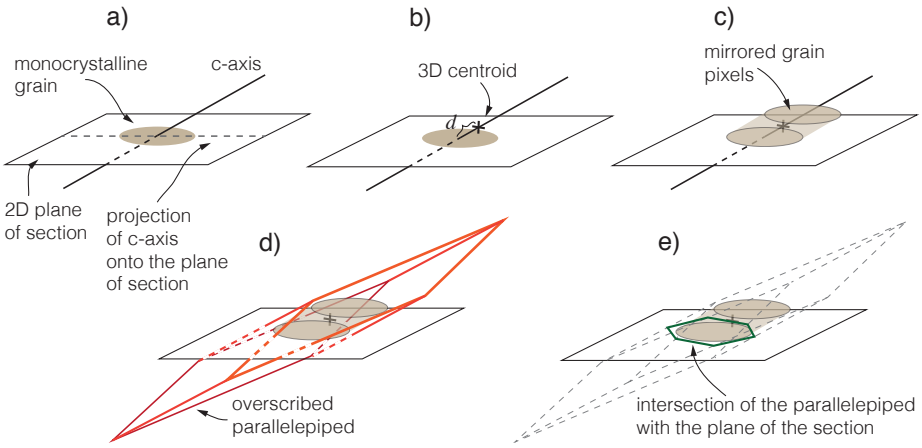

Figure B.22: The procedure leading to the determination of the bounding polygon for syntaxial cement growth: a) the c-axis direction is defined; b) the 3D centroid is determined; c) the grain pixels are mirrored about the 3D centroid to yield the surrogate 3D grain; d) three pairs of tangential planes are found; they constitute the bounding parallelepiped in 3D; e) the intersection of the parallelepiped with the plane of the porous medium is found.

After the direction of the c-axis is determined with the use of the rotation matrices (Figure B.22a), a 3D representation of the 2D grain is needed to find the three pairs of parallel planes of the bounding polyhedron. For that purpose a distance d is defined between the known centroid of the 2D grain and the unknown centroid of the surrogate 3D grain (Figure B.22b). This distance is selected from a normal distribution $N(0, \frac{\sqrt{A}}{10})$, where A is the area of the grain in pixels. In other words, the distance is sampled from a normal distribution with standard deviation of $\sigma = 0.3r$, where r is a length equivalent to a radius of a circle with the same area as the grain. The choice of distribution is arbitrary, but it is made on an assumption that it is likely that the 3D centroid is in close proximity to the 2D centroid visible in the section (normal distribution). Moreover, this choice ensures that the distance between the 3D and 2D centroids are at most equal to the equivalent radius r ($\sigma = 0.3r$), which is a natural assumption.

Following the determination of the distance d for a given grain, the vector $\vec{cc}$ pointing from the 2D centroid to the 3D centroid is calculated by rotating the vector $(0, 0, d)$ using the rotation matrices (R_x, R_y and R_z). The grain pixels are then mirrored by the means of translation by the vector $2\vec{cc}$. Figure B.22c shows the surrogate 3D grain which consists of the pixels of the original 2D grain and the mirrored pixels.

Appendix B.1.6. Tangent parallelepiped

The next step involves the determination of the bounding parallelepiped, which consists of three pairs of parallel faces tangential to the surrogate 3D grain (Figure B.22d). The first pair of parallel planes is found using the vector $\vec{n_1}$ and a formula for a plane crossing a point: $\vec{n} \cdot (\vec{x} - \vec{p}) = 0$, where $\vec{n}$ is the vector normal to the plane and $\vec{p}$ is the directional vector of the point. Point $\vec{p}$ is the centroid of the surrogate 3D grain, so that the resulting plane $N_1^{\vec{cc}}$ crosses the 3D centroid. To derive planes parallel to $N_1^{\vec{cc}}$ that are tangential to the grain, we proceed to calculate the distances between all vertices of the convex hull of the surrogate 3D grain and the plane $N_1^{\vec{cc}}$. The vertex $\vec{v_1^1}$ with the maximum distance from plane $N_1^{\vec{cc}}$ is the point that the first tangential plane $N_1^{\vec{v_1^1}}$ crosses. The coordinates of the vertex $\vec{v_1^1}$ and the normal vector $\vec{n_1}$ are used in the expression above to derive the equation of the tangential plane $N_1^{\vec{v_1^1}}$. We then proceed to calculate the distances between plane $N_1^{\vec{v_1^1}}$ and all of the vertices of the convex hull of the surrogate 3D grain. Again, vertex $\vec{v_1^2}$ with the maximum distance is the point crossed by the second tangential plane $N_1^{\vec{v_1^2}}$ and it is used to derive the equation of that plane.

This procedure is repeated for the remaining two pairs of parallel planes, using vector $\vec{n_2}$ to derive equations of planes $N_2^{\vec{v_2^1}}$ and $N_2^{\vec{v_2^2}}$ and vector $\vec{n_3}$ to derive planes $N_3^{\vec{v_3^1}}$ and $N_3^{\vec{v_3^2}}$. Finally, eight vertices of the parallelepiped are calculated as the points of intersection of eight combinations of three non-parallel planes using the formula:

$$\vec{x} = \frac{(\vec{x_1} \cdot \vec{n_1})(\vec{n_2} \times \vec{n_3}) + (\vec{x_2} \cdot \vec{n_2})(\vec{n_3} \times \vec{n_1}) + (\vec{x_3} \cdot \vec{n_3})(\vec{n_1} \times \vec{n_2})}{|\vec{n_1}\vec{n_2}\vec{n_3}|} \tag{B.6}$$

where $|\vec{n_1}\vec{n_2}\vec{n_3}|$ is the determinant of the matrix formed by the vectors normal to the planes and $\vec{x_1}, \vec{x_2}$ and $\vec{x_3}$ are the points that define the planes. These points are the set of vertices of the convex hull of the surrogate 3D grain found earlier in the procedure: $\vec{v_1^1}, \vec{v_1^2}, \vec{v_2^1}, \vec{v_2^2}, \vec{v_3^1}$ and $\vec{v_3^2}$.

Appendix B.1.7. 2D bounding polygon

Finally, the bounding polygon (Figure B.22e) is derived by intersecting the parallelepiped with the plane of the 2D medium (plane $z = 0$). The polygon is determined with the use of *intersectPlaneMesh* of the *geom3d-2014* toolbox [46]. The intersection between the parallelepiped and the plane can have a minimum of three sides and a maximum of six sides. The polygon constitutes the maximum bounds within which epitaxial growth can occur and syntaxial cement in Calcite2D is prohibited outside these bounds. However, due to obstacles encountered during growth in the form of impinging grains, only very rarely the full form of the polygon will develop.

To facilitate Stage 2 of the implementation (see Section Appendix B.2.3), the vertices of the intersection polygon most distant from each other are determined and a line passing through then is saved as one of the properties of the grain. Stage 1 is completed after a structure with all grain properties is saved.

Appendix B.2. Stage 2: cement growth

Once polycrystalline and monocrystalline grains are defined and the associated polygonal outer bounds of the epitaxial growth are established, the cement growth algorithm of Stage 2 of Calcite2D can be applied. Stage 2 takes the target width of the isopachous cement fringes β as an input parameter.

After the input porous medium and the grain properties structure is read, the first step in the code is a verification whether the sample percolates or not. A percolation check is performed in both directions (x and y). This is followed by an iterative process of growing a layer of cement 1 pixel thick until no cement is produced anymore. In the case of the isopachous cement, that stopping point is determined by the input β to Stage 2 code. In this study values from 0 to 10

pixels are used. When the target width of isopachous cement fringes (β) is set to the maximum value used in this study: 10 pixels (an equivalent of $50\mu m$), 10 iterations of Stage 2 of Calcite2D are necessary to grow all of the isopachous cement.

The maximum possible extent of the syntaxial cement is determined by the bounding polygons, which are established in Stage 1. Although the outer bunds of syntaxial cement are determined in Stage 1, the *volume* of syntaxial cement cannot be determined before Stage 2 is completed. This is because the *hypothetical* extent of syntaxial cement delineated by the maximum bounds is often not achieved due to the effect of grains impinging on one another. Syntaxial cement for a given grain stops growing either when the entire bounding polygon is filled, or when all seeding sites of the grain are blocked by impinging grains. Syntaxial growth in the entire medium ceases when all grains have reached that point. The amount of iterations necessary to achieve that point depends on the size of the bounding polygons, which is controlled by the size of the monocrystalline grains, and on the arrangement of the grains with respect to each other (the impinging potential). In general, Stage 2 takes a significant number of iterations until completion (in this study usually up to 100, but sometimes more than 200) and this number cannot be accurately determined before the simulation.

Appendix B.2.1. Isopachous cement growth

Firstly, 1 pixel layer of isopachous cement is grown around all polycrystalline grains, but only if the target width of the isopachous cement fringes β has not been achieved yet. The growth involves an iterative procedure on all outline pixels of each polycrystalline grain. For each of the outline pixels, the pixels in its 4-connected neighbourhood (north, south, east and west) are investigated in terms of their type (whether they are pore or solid). If a neighbouring pixel is found to be a pore pixel, it is turned into a solid (cement) pixel. If it is found to be a solid pixel, it means that an obstacle is encountered and that pixel is not available for cement growth for that grain. After this procedure is completed

for all outline pixels of the grain, grain properties are updated with the new isopachous cement layer for that grain.

The iteration on all outline pixels is repeated for all of the polycrystalline grains and upon its completion the porous medium matrix is updated with the new layer of isopachous cement.

Appendix B.2.2. Syntaxial cement growth

The following steps and rules are followed for each monocrystalline grain in each iteration of Stage 2:

1. If a grain is monocrystalline and still active, i.e. it has grown cement in the previous iteration, steps 2 through 4 are followed for all outline pixels of that grain.
2. If an outline pixel is within the bounds of the current bounding polygon, investigate all 4-connected neighbouring pixels of that grain (north, south, east and west) in terms of their type (pore of solid).
3. If the neighbouring pixel is a pore and lies within the bounding polygon, it becomes a solid (cement).
4. If any of the neighbouring pixels is solid *and* belongs to another grain, implement 'impinging' effect to update the bounding polygon (details in a Section below).
5. After all outline pixels of a grain have undergone this procedure, update the grain properties with the new syntaxial cement.
6. If no new cement is added for a grain in a given iteration, deactivate the grain (implemented for runtime efficiency).
7. After iteration is completed for all monocrystalline grains, update the porous medium with the new cement.

Appendix B.2.3. Impinging grains and the 'shadow' effect

As mentioned in Section 1.2.5, the impinging effect, where grains create compromise boundaries and block each other's seeding sites, and the 'shadow' effect, where the cement behind an obstacle is not grown because non-euhedral

seeding sites have been blocked, are observed in natural carbonate rocks (J.A.D Dickson, pers. comm). Calcite2D implements these effects by noting that every time an obstacle pixel is encountered, the area in its 'shadow' is of the form of a parallelogram with edges parallel to the two closest sides of the bounding polygon sides. The bounding polygon is adjusted by removal of that parallelogram. This is achieved by replacing the vertices of the bounding polygon that are in the 'shadow' with new points.

Figure B.23 illustrates the intricacies of the 'shadow' effect implementation. Polygon vertices that are in the 'shadow' are found and replaced in a correct order with new points. First, all lines going through the outline point that encountered the obstacle (P_{fail}) and parallel to polygon edges are calculated as well as the points of intersection of these lines with the edges of the bounding polygon. For each of these lines only the intersection point closest to P_{fail} is considered (Figure B.23a). The number of these points depends on the number of the edges of the bounding polygon and can vary from 2 to 3. All new vertices of the updated polygon are among these intersection points.

In order to aid the elimination of the points that are not to be the vertices of the updated bounding polygon from the set of the intersection points, a list of intersection points properties is made. This list includes: 1) the distances between the intersection point and P_{fail}, 2) the polygon edge number the point lies on and 3) the point coordinates. Following that, a line passing through P_{fail} and the grain centroid is calculated and the line perpendicular to it a small distance away from P_{fail} towards the grain centroid is determined (the 'perpendicular' line). The intersection points that lie on the opposite side of the perpendicular line to P_{fail} are eliminated from the list of potential new vertices of the updated polygon (Figure B.23b).

This finalises the list of the new vertices. All that remains is the determination of the correct order in which they are to be inserted in the list of bounding polygon vertices (a grain property), and the determination of the polygon vertices to be replaced by them, as they are in the 'shadow'. The list of eligible intersection points has a maximum of two points and there are several cases

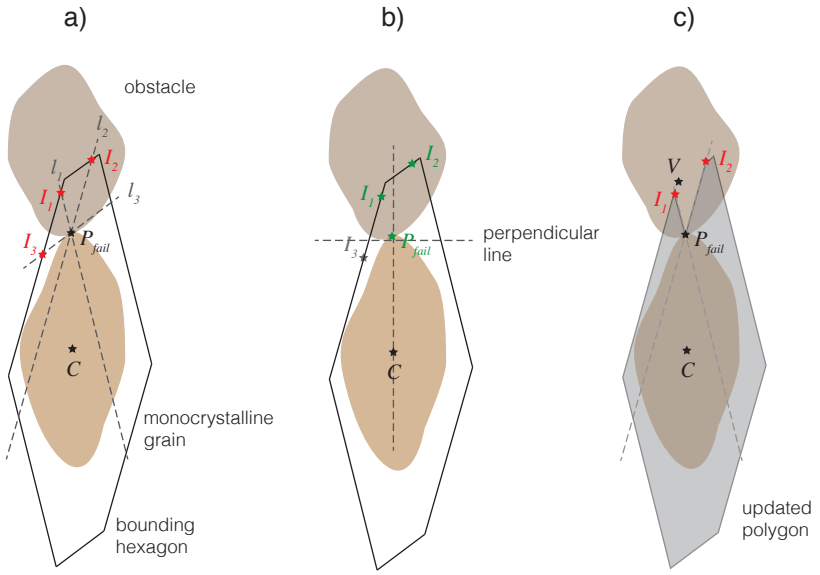

Figure B.23: The steps in the implementation of the impinging and 'shadow' effects: a) the lines through the point that encounters the obstacle (P_{fail}) that are parallel to the edges of the bounding polygon, l_1, l_2 and l_3, intersect the sides pf the polygon at points I_1, I_2 and I_3 respectively (red); b) only the intersection points on the same side of the perpendicular line as P_{fail} (green) are considered; c) the remaining intersection points I_1 and I_2 (red) together with P_{fail} replace vertex V that lies in the 'shadow' zone to yield the updated bounding polygon.

that need to be investigated. If both of these intersection points lie on the same edge of the current bounding polygon, it means that no current bounding polygon vertex is in the 'shadow' and no action is necessary. If the intersection points lie on two different edges, then at least one of the vertices of the current bounding polygon lies in the 'shadow' zone. Depending on the edges the intersection points lie on, i.e. whether they are two consecutive edges of the polygon or not, the current polygon vertices connecting these edges are replaced with three points: I_1, P_{fail}, I_2. This results in an updated bounding polygon (Figure B.23c).

Figure B.24 illustrates the result of the impinging and 'shadow' effect as implemented in Calcite2D. In a very simple synthetic porous medium with three monocrystalline grains two of them encounter obstacles during the growth. The bounding polygons are adjusted accordingly to accommodate the effect of the obstacles and the resulting cement volume is diminished by the volume denoted by green stars.

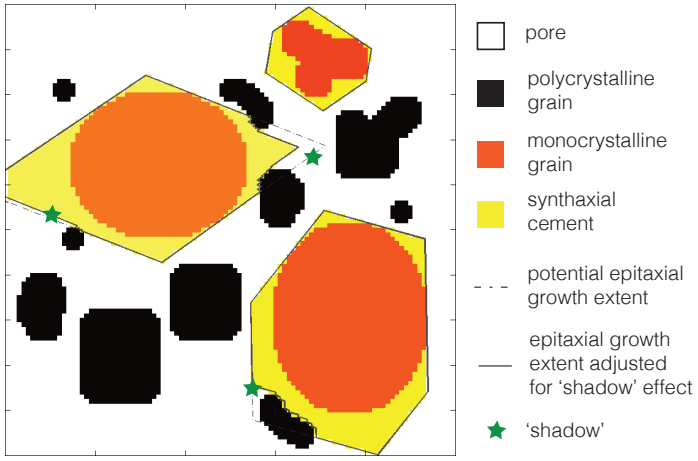

Figure B.24: The 'shadow' effect implemented in Calcite2D illustrated in a simple synthetic medium of size 100^2 pixels.

Appendix B.2.4. Finishing steps

For runtime efficiency purposes, only the outlines of all grains are updated at the end of each cement growth iteration, i.e. the interiors of the grains are not

considered. Before all outputs are saved, it is investigated whether the medium still percolates in both directions (x and y).

The entire procedure detailed in Section Appendix B.2 is repeated until no cement is produced in an iteration.

Appendix C. Details of the Implementation of the Deposition Model in 3D

Appendix C.1. 2D data from a segmented thin-section

The 3D deposition model aims to mimic the same carbonate rock type as is used in the 2D modelling, so the same thin-section image is used. The thin-section image (Figure 3a) is segmented and stripped of cement, following the methodology detailed in Section 2.1.1. The binary back-stripped image (Figure 3b) is then used to extract a joint distribution of grain shapes and sizes using Matlab's Image Processing Toolbox (function *regionprops*). Only the grains fully visible in the 2D image are considered. Inclusion of grains interrupted by the boundaries of the image could result in lowering of the average size of grain, and a shape distribution skewed towards the more elongated shapes. Excluding these incomplete grains avoids this bias. Of the 604 grains in the binary back-stripped image, 81 are incomplete, i.e. touching a boundary of the image, and 523 are completely visible.

The shape parameter is the aspect ratio of the grain. More specifically, it is the eccentricity of the ellipse with the same second-moments as the section of the grain visible within the plane of the image. The size parameter is the length equivalent to a diameter of a circle with an area equal to the area of the section of the grain (the equivalent diameter).

Figure C.25a shows the shape and size data for the 523 complete grains visible in the binary back-stripped image as well as a probability density function of the two variables obtained with the use of the kernel density estimation [47]. The obtained probability density function is subsequently used to generate a sample of 6000 pairs of grain shape and size variables, as shown in Figure C.25b.

The generated sample has a probability distribution almost identical to the distribution of the grain shape and size parameters in the binary back-stripped image.

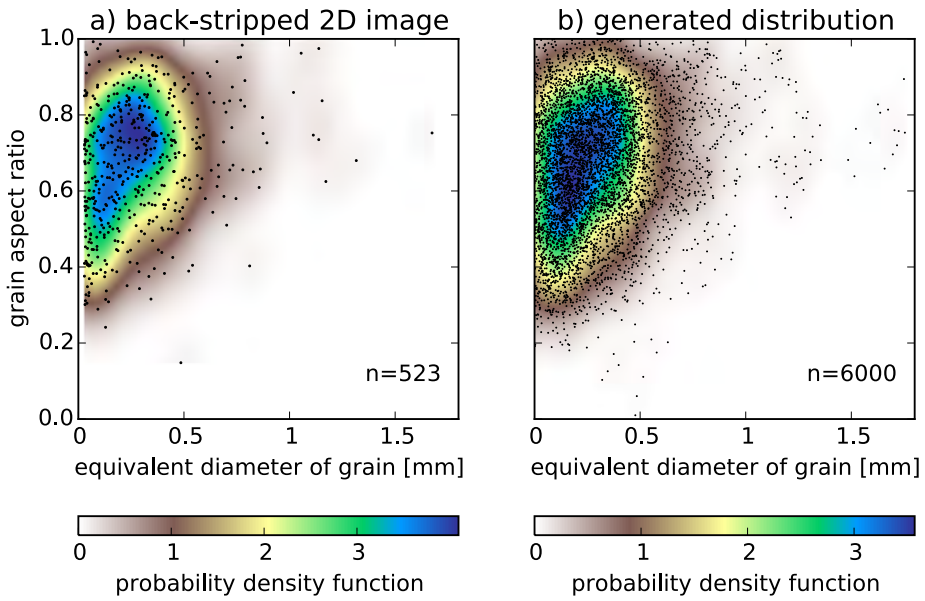

Figure C.25: Joint distributions for grain size and shape for a) 523 complete grains visible in the binary back-stripped image, b) the sample generated using the kernel density estimation on the distribution in the back-stripped image. The grain shape parameter is the eccentricity of the ellipse that has the same second-moments as the section of the grain visible in the 2D plane. The grain size parameter is the equivalent diameter of a circle with the same area as the grain.

Appendix C.2. Deposition simulation

The generated sample of grain sizes and shapes is used to create a grainstone deposit. Grains are created and simulated in Blender, a free and open-source 3D creation suite [28]. The grains are initially created in the form of spherical meshes with 42 vertices and 80 triangular faces and a diameter specified by the size variable from the generated sample (the equivalent diameter). Their shape is subsequently modified by reducing two of the axes of the sphere so that the ratio of the two minor axes of the resulting ellipsoid to the major axis is equal to the shape parameter from the generated distribution (the eccentricity). Next,

the grain meshes are randomly rotated, so that there is no bias arising form the pre-simulation orientations of the elongated grains.

In addition, an impenetrable static box is created with a base of 4×4mm and a height of 5mm, in which the grains will be deposited. 1904 grains are created and arranged in 119 layers of 4×4 grains directly above the box, spaced so that they do not intersect with each other.

The open-source Bullet Physics Engine [27], incorporated in Blender, is then used for simulation of the physical interactions of grains falling and settling due to gravity. Bullet Physics implements gravity and collision physics and is a well established physics engine used for scientific modelling as well as game programming. For the purposes of the simulation, grains are treated as rigid bodies, which ensures that they do not deform when they collide with other objects. The friction coefficient is set high (0.9) so that the grains behave like natural grains, which seldom have smooth surfaces. A high damping coefficient (0.9) as well as a high rotation damping coefficient (0.9) are used to mimic the environment of deposition in a fluid, as opposed to deposition in air, which is characterised by a relatively small damping of movement. Lastly, a mass proportional to d^3, where d is the size parameter from the generated distribution (the equivalent diameter), is applied to each grain. This ensures that the grains have a momentum proportional to their mass, thus larger grains have more impact in case of collision with smaller grains, just like in the physical world.

Figure C.26a shows the state of the grains after the physics simulation in Blender is completed and 1904 grains have fallen and been deposited in the box of dimensions $4 \times 4 \times 5$mm. The output of the model is a mesh-based grain accumulation structure, i.e. the grains are described by a set of vertices and faces. The grains are subsequently saved in a Wavefront.obj format, which contains the coordinates of the vertices and faces of each grain.

Appendix C.3. Voxelised 3D porous medium

Before the product of the simulation of the settling grains can be used as an input in the cementation model, the grain packing needs to be post-processed.

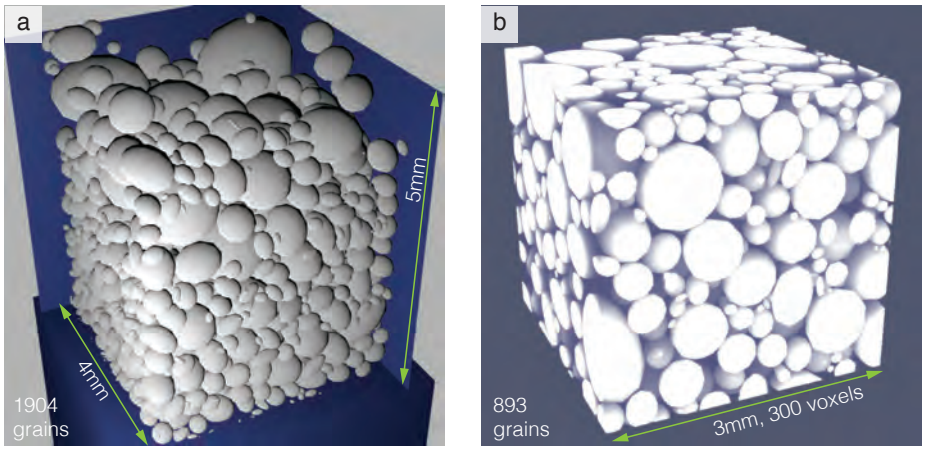

Figure C.26: The model output of the deposition simulation: a) the end-state of the physics simulation using Bullet Physics Engine in Blender, 1904 grains (white) are deposited in a $4 \times 4 \times 5mm$ box (blue); b) post-processed synthetic deposit ready for cement simulation, grain packing in mesh representation is cropped to $3mm^3$ and voxelised to 300^3 voxels so that only 893 grains (white) remain.

The procedure starts with reading the output of the grain deposit simulation in the form of meshes (Figure C.26a) into Matlab using a function *read_wobj* [48]. A structure containing all grains is created, including the coordinates of 42 vertices and a list of 80 faces for each grain. The vertices and faces are retained as properties of each grain to be used in the cementation model.

In order to avoid artefacts in the arrangement of the grains arising from the proximity of the grains to the sides of the deposit box, the original deposit of dimensions $4 \times 4 \times 5$mm is cropped by 0.5mm from all sides except from the top, where it is cropped by 1.5mm. The deposit is cropped mainly from the top, because this area has a tendency to be uneven, as opposed to all the other sides, which are controlled by the sides of the deposit box. Cropping the top by 1.5mm ensures that no empty spots are captured. This procedure yields a porous medium of dimensions $3 \times 3 \times 3$mm and with a smaller number of grains.

Since both Calcite3D and the Lattice Boltzmann method require a voxelised medium as an input, the grains are then converted from a mesh to a voxel representation. The voxelisation of the mesh is achieved by choosing the number of voxels in each dimension. In this study the size of 300^3 voxels is chosen, which,

combined with the porous medium of dimensions $3 \times 3 \times 3mm$, results in a voxel size of $10\mu m$. This is twice as big as the pixel size in the 2D study.

After all coordinates of vertices of grain meshes are converted from Blender units to grid units, each grain is voxelised. This is achieved by finding the extrema of the grain mesh in three dimensions so as to determine the smallest box with faces parallel to the faces of the 3D porous medium that can be circumscribed on the grain. Next, all grid points in the enclosing box are investigated as to whether they are located inside or outside of the grain mesh using function *inhull* by [49]. The grid points inside the grain mesh are designated as solid voxels and the ones that are outside - as pore voxels. Figure C.26b shows the cropped porous medium voxelised to a 300^3 voxel grid.

Appendix D. Details of the Implementation of Calcite3D

Appendix D.1. Stage 1: grain labelling and crystal axes definition

The procedure starts with the reading of the inputs. This consists of a structure with grain properties including a mesh representation of a grain, i.e. the coordinates of vertices and the list of faces, and a set of voxels belonging to that grain as well as the voxelised 3D porous medium, which differentiates between pore and solid voxels.

Appendix D.1.1. Grain labelling

The grains are labelled either monocrystalline of polycrystalline, based on the input parameter α_0 and a random number generator, so that the final content of monocrystalline grains (α_n) might differ slightly from the model input parameter.

Appendix D.1.2. 3D bounding polyhedron

For each monocrystalline grain the circumscribed crystal is determined. This is achieved following the methodology to find a tangent parallelepiped on a surrogate 3D grain described in Section Appendix B.1. The difference is that instead of the surrogate grain, vertices of the mesh representation of the actual

3D grain are used. The technical details involved in this methodology are presented in Section Appendix B.1 and what follows here is only a short description of the steps followed.

The orientation of the crystal axis of the monocrystalline grain is selected at random by rotating the planes associated with a rhombohedral form of calcite (either $01\bar{1}2$ or $40\bar{4}1$) in three directions using the rotation matrices. Afterwards, the six planes tangential to the grain are found. The intersections of the planes define the bounding parallelepiped which delineates the maximum potential extent of syntaxial cement growth for that grain, pending impinging effects.

Appendix D.1.3. Other grain properties

To facilitate Stage 2 of the cementation model, the grain properties are supplemented with a list of faces that bear a given vertex and a list of vectors normal to the faces of the grain (performed using the function *patchnormals* developed by [50]). All grains are then given an 'active' label. The two most distant vertices (extrema) of the bounding polyhedron are found and retained as a pseudo c-axis of the grain. The extrema are used in the implementation of the impinging and the 'shadow' effects (details below).

Appendix D.1.4. Representations of the content of monocrystalline grains: α_n, α_v and α_a

After all grains are labelled, the number of the monocrystalline grains is calculated, which enables the derivation of the ratio of the number of monocrystalline grains to all grains (α_n). The volume of monocrystalline grains in voxels is also determined, so that the ratio of the volume of the monocrystalline grains to the volume of all grains (α_v) can be determined. Finally, the surface area of all grains is determined using the mesh representation of the grains and the package *geom3d* [46], so that the ratio of the surface area of the monocrystalline grains to the surface area of all grains (α_a) can be calculated.

Appendix D.1.5. Outputs

The outputs saved at the end of Stage 1 of Calcite 3D include:

- A 3D porous medium matrix that differentiates between pores, monocrystalline and polycrystalline grains;
- A grain structure with grain properties common to both types of grains:
  - the coordinates of grain vertices and a list of faces;
  - a set of grain voxels;
  - a list of vectors normal to grain faces;
  - a list of faces which bear a given grain vertex;
  - an active/inactive label;
  - a monocrystalline/polycrystalline label;
- Grain properties exclusive to monocrystalline grains:
  - the coordinates of the centroid of the grain;
  - the plane orientations associated with the bounding parallelepiped;
  - the coordinates of of the vertices the bounding parallelepiped and a list of its faces;
  - the coordinates of the two most distant vertices (extrema) of the bounding parallelepiped.

Finally, all bounding parallelepipeds (crystals) are voxelised and saved as an output to be used in Stage 2 of Calcite3D. The voxelisation procedure is memory-intensive, as the voxel volume of all bounding polyhedra might many times exceed the volume of the 3D medium (300^3 voxels), particularly in the high-monocrystalline grain content cases (high α_0). However, this is implemented to accelerate Stage 2 and avoid many *inhull* calls, which are time-consuming.

Appendix D.2. Stage 2: cement growth

Once the polycrystalline and monocrystalline grains are defined and the associated polyhedral outer bounds of the epitaxial growth are assigned to them,

the cement growth algorithm of Stage 2 of Calcite3D can be applied. Stage 2 takes the target width of the isopachous cement fringes (β) as an input parameter.

After the outputs of Stage 1 are loaded, the first step of Stage 2 determines whether the 3D porous medium percolates in all three directions. If the code is run for the first time, the simulation time is initialised to 0 and the current width of the isopachous cement fringes is set to 0. If the simulation is restarted, the current time step and the current width of the isopachous cement fringes are loaded from the last save point of Stage 2. The cement growth is then started, first with 1 voxel layer of isopachous cement growth on the polycrystalline grains, followed by a layer of syntaxial cement growth around the monocrystalline grains.

Similarly to Calcite2D, the isopachous cement growth stops as soon as the target width of isopachous cement fringes is reached, as set by an input β to Stage 2. In this study, values from 0 to 5 voxels are used, which means that a maximum of 5 iterations are necessary to grow the isopachous cement fringes to a thickness equivalent of 50 μm.

Note that the maximum possible volume of the syntaxial cement is determined by the bounding polyhedra found in Stage 1. The syntaxial cement for a given grain stops growing either when the entire bounding parallelepiped is filled, or when all seeding sites of the grain are blocked by impinging grains. The syntaxial cement growth in the entire medium ceases when all grains have reached that point. The amount of iterations necessary to achieve that point depends on the size of the bounding polyhedra, which are controlled by the size of the monocrystalline grains, and on the arrangement of the grains with respect to each other (the impinging potential). Stage 2 takes a significant number of iterations until completion (in this 3D study usually up to 100) and this number cannot be accurately determined before the simulation.

Appendix D.2.1. Isopachous cement growth

If the current width of the isopachous cement fringes is smaller than the target width specified by the input to Stage 2 of Calcite3D (β), the following steps are repeated for all polycrystalline grains:

1. Expand the mesh of the grain by translating all faces of the grain outward by 1 voxel (Figure D.27a). This is achieved by translating each face along its normal (a grain property) by a length of 1 voxel and deriving the new plane using the equation of the plane passing through a point. The list of faces that each grain vertex is on (a grain property) is then used to determine the points of intersection of the expanded grain mesh. Grain properties are then updated with the new vertices.

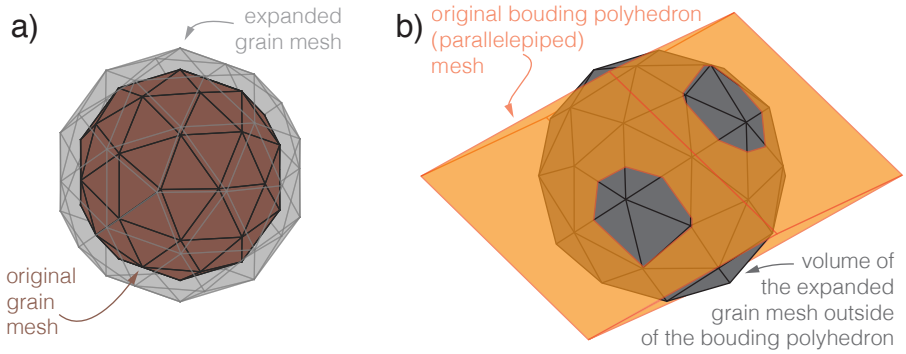

Figure D.27: a) The grain mesh is expanded by translating all the faces outward by 1 voxel. b) The bounding polyhedron is circumscribed on a monocrystalline grain. New cement is added only in the intersection zone of the expanded grain and the bounding polyhedron.

2. If a grain is active, determine the set of voxels that are in the expanded grain, but not in the original grain - this set of voxels is the potential new isopachous cement. This is achieved by voxelising the expanded grain using the same method as described earlier to voxelise each grain of the synthetic sample (see Section Appendix C.3).
3. From the set of the voxels contained in the expanded grain, remove the voxels that are also contained in the original grain.
4. From the obtained set of voxels in a form of a 1-voxel-thick shell, remove

the voxels that are already designated as solid, i.e. the voxels that belong either to another grain or to cement, as of the previous iteration of cement growth. The voxels that remain in that set are the new isopachous cement for that grain produced in that iteration.

5. If that set is empty, i.e. if no isopachous cement is produced for that grain in the current iteration, deactivate the grain.
6. Otherwise update the porous medium matrix with the new isopachous cement and update the properties of the grain to include the new cement.

After the procedure is repeated for all polycrystalline grains, the volume of isopachous cements found in this iteration is determined and the current width of the isopachous cement fringes is increased by 1.

Appendix D.2.2. Syntaxial cement growth

If there are any active monocrystalline grains left, i.e. if any monocrystalline grain produced a non-zero volume of the syntaxial cement in the previous iteration, repeat the following steps for all monocrystalline grains:

1. If a grain is active, expand the grain mesh, just like in the case of the isopachous cement growth (Figure D.27a).
2. Voxelise the expanded grain and remove from that set voxels belonging to the original grain, so as to form 1-voxel-thick shell of voxels. Any new syntaxial cement that is going to be produced for that grain in that iteration is in that set of voxels.
3. Remove from that set any voxels that lie outside of the bounding polyhedron (Figure D.27b). This is achieved with the use of the *inhull* function.
4. For each of the voxels form the resulting set, verify whether they are already solid, i.e. are in another grain of cement as of the previous iteration. This is achieved by investigating the entries in the 3D porous medium matrix. The voxels that are found to be already solid are the 'obstacle' voxels and for each of them the following steps implementing the impinging effect are followed:

(a) Find the 'extremum' of the bounding polyhedron of the grain (a grain property) that is closest to the 'obstacle' voxel.

(b) Calculate *three* planes with orientations equivalent to the orientations of the faces of the bounding polyhedron (a grain property) and which are crossing the 'obstacle' point/voxel.

(c) Determine the *three* planes of the bounding polyhedron that meet at the closer 'extremum' of the bounding polyhedron.

(d) Intersect eight triplets of non-parallel planes of these *six* planes to obtain eight vertices of a parallelepiped (Figure D.28a). This parallelepiped is the 'shadow' parallelepiped that is prohibited from growth by the fact that it is blocked by the 'obstacle' point.

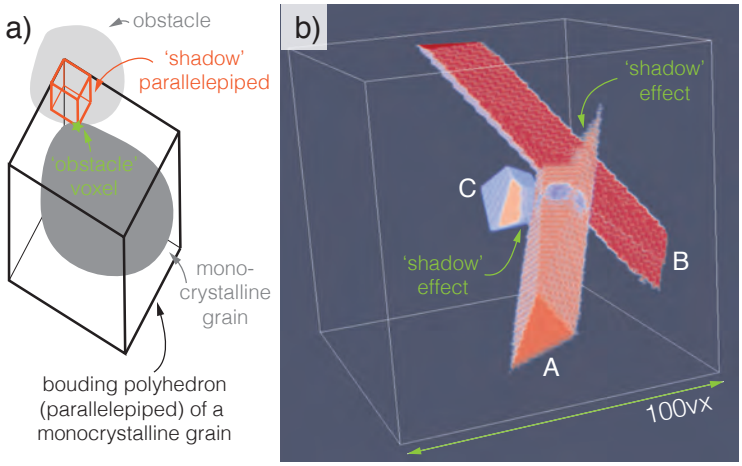

Figure D.28: The impinging effect. a) Syntaxial cement growing around a monocrystalline grain encounters another grain at an 'obstacle' point (green star). As a result, the voxels inside of the 'shadow' parallelepiped (red) are removed from the list of the potential syntaxial cement voxels. b) The impinging and 'shadow' effects implemented in Calcite3D. Three monocrystalline grains, which developed syntaxial cement of the crystal form $40\bar{4}1$, are voxelised in a 100^3 voxel box. Syntaxial cement grown on these grains impinges on one another and the cement volume is limited.

(e) From the set of voxels describing the current maximum extent of syntaxial cement growth, i.e. the current state of the bounding polyhedron modified by any previous impinging effects, remove the voxels that lie within the 'shadow' parallelepiped. This updates the maximum possible extent of the syntaxial cement growth for that grain.

5. From the set of the potential syntaxial cement voxels for that grain, remove the ones that are not in the set of the voxels belonging to the updated bounding polyhedron. This completes the removals of voxels from that set as only the voxels that constitute the new syntaxial cement now remain.
6. If this set is empty, i.e. if no new syntaxial cement is produced for that grain in that iteration, deactivate the grain.
7. Otherwise update the 3D porous medium matrix with the new syntaxial cement and update the grain properties to include the new cement and the updated set of voxels of the bounding polyhedron.

After the procedure is repeated for all monocrystalline grains, the volume of syntaxial cements found in this iteration is determined.

Appendix D.2.3. Impinging grains and the 'shadow' effect

The idea behind the implementation of the impinging effect, as described in the previous section, is the same as in the case of the 2D model (see Section Appendix B.2.3). It is based on an observation that when syntaxial cement encounters an obstacle during its growth, that 'obstacle' point is blocked and will not seed any more cement (Section 1.2.5). Thus a 'shadow' is created where no syntaxial cement can be produced by that grain. In the 2D case this 'shadow' takes a form of a parallelogram (Figure B.23), while in the 3D case it takes a form of a parallelepiped (Figure D.28a).

In the 2D model it is possible to retain the representation of the bounding polygon in a form of its vertices and edges and implement the impinging effect based on that representation. However, due to the increased complexity, in the 3D model it is not possible to implement the effect of impinging using the mesh representation of grains. This is the main reason why a voxel-based approach is chosen, even though memory and run time requirements are significantly larger.

Figure D.28b shows a result of the implementation of the impinging effect on an example of three monocrystalline grains with syntaxial cement of the crystal form $40\bar{4}1$ voxelised in a 100^3 voxel box. Grain B blocks grain A from growth (green arrow), so that only a small seeding area remains. Grain A impinges

on grain C and reduces the volume of the syntaxial cement produced (green arrow).

Appendix D.2.4. Finishing steps

Once cement is grown for every active monocrystalline and polycrystalline grain, the updated porosity of the 3D porous medium due to the new isopachous and syntaxial cements produced in a given iteration is determined. The simulation time is increased by 1 and all outputs are saved, including the 3D porous medium matrix (which serves as the input for flow simulation), the current state of the grain properties (for the purposes of restarting the simulation in case it is interrupted) as well as the isopachous cement and the syntaxial cement volume produced in each iteration.

Appendix E. Lattice Boltzmann simulation set-up

The boundary conditions applied to the porous media in the 2D study include the Zou-He pressure boundary [51] on the inlet and outlet sides of media, and a 'bounce-back' fully reflective boundary on the sides parallel to the direction of the pressure gradient. The Zou-He pressure boundary is chosen to minimise the computational cost of the simulation. An alternative to the Zou-He boundary is a periodic boundary, where the fluid exiting the outlet of the domain immediately re-enters the domain at the inlet and the fluid is forced by the application of velocity at the acceleration zone in the inlet. However, the use of a periodic boundary condition on the inlet and outlet of computational domain requires that the medium is either mirrored about the outlet, so that its length doubles [8], or that a buffer zone is added on both sides of the medium [52]. In both cases the computational domain is increased and so does the simulation time. The Zou-He pressure boundary condition was found to yield reliable prediction of permeability at a lower computational cost [51].

The choice of the 'bounce-back' boundary condition for the other sides of the domain was made due to two reasons. Firstly, this computational set-up mimics the experimental set-up for the measurement of permeability, where a

core plug is enclosed from all sides except for the direction in which fluid is forced. Secondly, the alternative - a periodic boundary - works best if the pore and solid pixels across the boundary correspond to each other. This can be achieved e.g. by mirroring of the medium. However, if we were to mirror the medium in all three dimensions, it would increase the domain eight times, which would be computationally prohibitive. Moreover, such mirroring of the sample would introduce correlation into the flow simulation, which would artificially increase flow and the permeability prediction. Substituting buffer zones (as mentioned above) for mirror images of the computational domain is only a viable option on the faces perpendicular to the fluid flow. The introduction of such buffer zones on the faces of the medium parallel to the flow direction would result in almost all flow converging to these buffer zones and little of the fluid flowing through the actual sample. The outcome would be a useless result of a very high permeability.

Another alternative to mirroring of the computational domain is to design the medium in such a way that the pore spaces across the faces of the medium parallel to the pressure gradient correspond to one another exactly [33]. However, manipulation of the cemented synthetic sample in order to force the inlet and outlet pores to correspond to one another would interfere with the integrity of the fabrics generated by Calcite2D, which is an undesired effect. On the other hand, if a periodic boundary condition is used across a boundary where pore and solid pixels do not match, unnatural pore geometries often occur leading to artefacts in the flow. The use of the 'bounce-back' boundary condition avoids these issues and is realistic for comparison of simulation with lab results.

The pressure difference between the inlet and outlet boundaries across the 2000^2 pixel sample was set to 0.1. This was determined through test-simulations to be a satisfactory compromise between the time to convergence (boosted by high pressure) and absence of turbulent flow and computational stability (promoted by low pressure). The relaxation parameter τ used in this study is 1, a value most commonly used in the literature [52]. In the single-relaxation LB scheme, as the one used in this study, permeability calculation is known to

depend on the relaxation parameter τ.

In the 3D study the simulation set-up is the same as in the 2D study, with the Zou-He pressure boundary [51] on the inlet and the outlet faces of the 3D porous medium and a bounce-back boundary on the faces parallel to the direction of the pressure gradient are used. The pressure difference chosen between the inlet and outlet boundaries is 0.1 across the 300^3 voxel medium. The relaxation parameter τ used in this study is 1.

Appendix F. Permeability calculation

Permeability is computed using the outputs for the density and the velocity of the fluid in the direction of the pressure gradient (fluid forcing direction) according to the formula [37, 33]:

$$\kappa_{LB} = \nu \frac{\langle U_x \rangle}{\bigtriangledown P} \tag{F.1}$$

where $\bigtriangledown P$ is the pressure gradient across the sample, calculated as the difference between the average density at the inlet pores and the average density at the outlet pores (0.1) divided by the size of the sample in grid units (2000 in the 2D study and 300 in the 3D study); $\langle U_x \rangle$ is the average fluid velocity in the flow direction across the entire sample (pores as well as solids); ν is the kinematic viscosity of the sample and is equal to $\frac{\tau - 0.5}{3}$ in both the D2Q9 and D3Q27 implementations of the LB method used in the 2D and 3D modelling respectively [41], where τ is the time relaxation parameter equal to 1 in all simulations. The relaxation parameter can be calibrated to achieve more accurate permeability predictions. Usually it is calibrated to the analytical Hagen-Poiseuille flow in a pipe [52]. As this study focuses on the differences in permeability between various realisations of a synthetic cemented rock, careful calibration of the relaxation parameter is not employed, as an order of magnitude prediction of permeability is sufficient.

The conversion of κ_{LB} from lattice units to physical units is done according to the formula: $\kappa_{m^2} = \kappa_{LB} \cdot r^2$, where the r is the resolution of the porous

medium used in the simulation ($5\mu m$). The resulting permeability in the units of m^2 is converted to the more common mD with the formula: $\kappa_{mD} = 1000 \cdot \frac{\kappa_{m^2}}{9.869233 \cdot 10^{-13}}$. The treatment of units is exactly the same in the 2D and 3D simulations, as the 2D sample is effectively treated as a 3D sample, where one of the dimensions (the depth) is equal to 1 lattice unit.

The amount of iterations of the LB simulation necessary to achieve a steady state (convergence) varies depending on the nature of the porous medium. Generally, flow simulation in samples with high porosity tends to converge faster than in samples with low porosity. In the 2D study all simulations are run for 1,000,000 iterations and partial output is saved every 5,000 iterations, so that the convergence can be confirmed. Figure F.29 illustrates a sample with porosity 30.5% for which Lattice Boltzmann simulation is run and Figure F.30 shows that convergence has been achieved by the end of the simulation. In all simulations run in the 2D study the difference in permeability between the last two iterations with saved partial output (i.e. iteration 1,000,000 and 995,000) is less than 0.7%. As LB convergence for samples of low porosity (and generally low permeability) progresses slower than for the high porosity samples, that difference in permeability is smallest for high porosity/permeability samples and increases for lower permeability samples. The mean difference in permeability between iterations 1,000,000 and 995,000 for samples with κ higher than $1000mD$ is 0.005%, for samples with κ between 100 and $1000mD$ is 0.1%, and for samples with κ less than $100mD$ it is 0.13%.

Similarly, in the 3D modelling, synthetic samples with high porosity tend to converge faster than the samples with low porosity. Samples with porosity of about 12% typically require about 100,000 iterations to achieve convergence, while samples with porosity of about 30% can reach convergence even after 20,000 iterations. Figure F.31 illustrates a synthetic sample with porosity 12.4% for which Lattice Boltzmann simulation was run for 100,000 steps (about 570 CPU hours).

In order to obtain a more accurate permeability prediction, mostly for the benefit of the low porosity/permeability samples, an exponential convergence

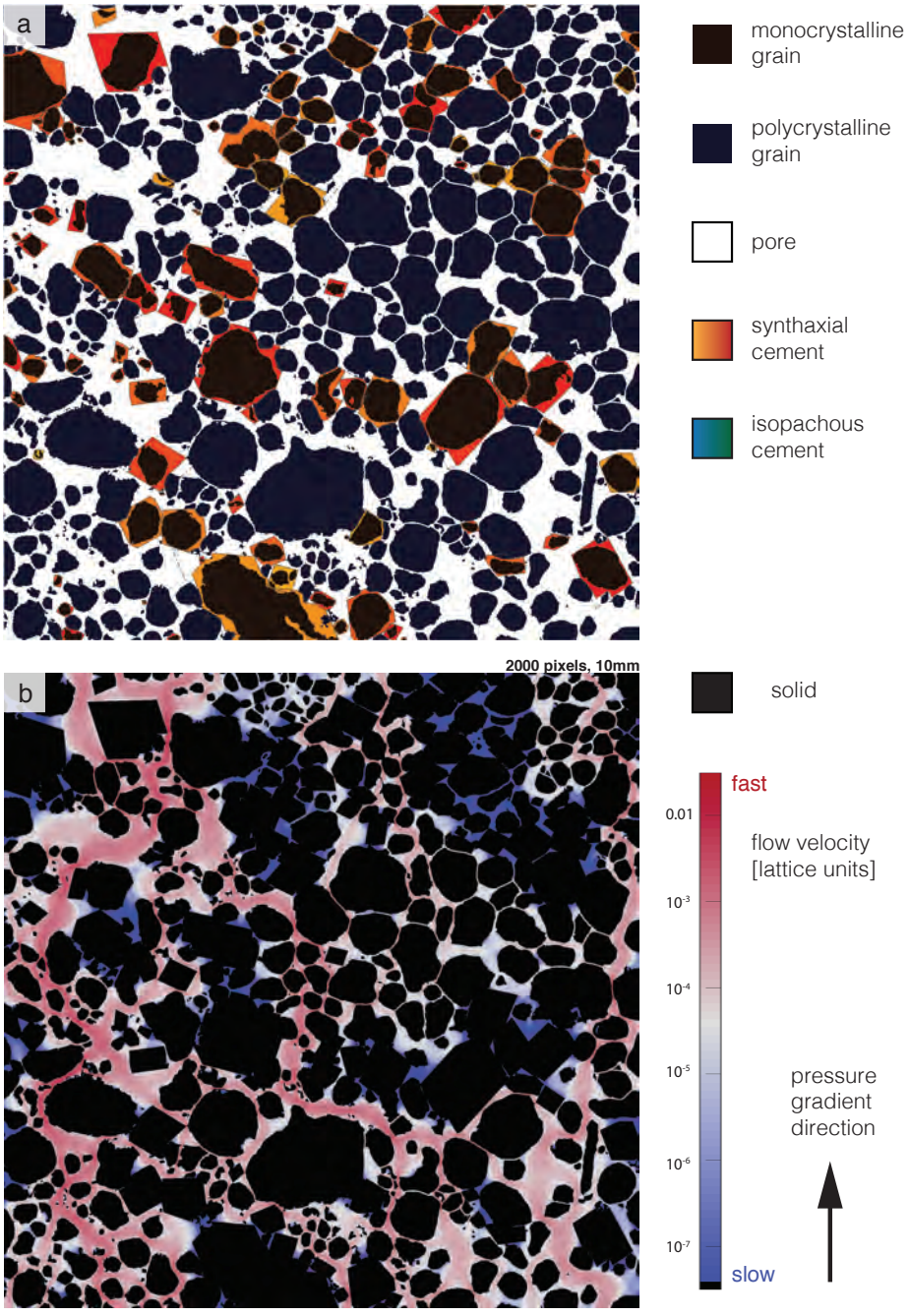

Figure F.29: A model output of Calcite2D (a) with an associated result of the LB flow simulation (b); a) cemented synthetic sample with crystal form $01\bar{1}2$ obtained using model input parameters $\alpha_0 = 0.21$ and $\beta = 0$ pixels and a porosity $\phi = 30.5\%$, b) log of the magnitude of flow velocity for the same sample ($\kappa = 3200mD$).

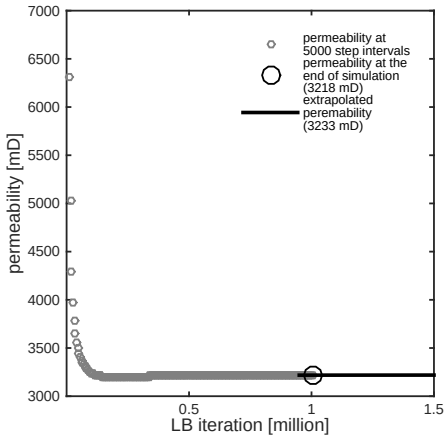

Figure F.30: The convergence of permeability in a LB simulation in the sample shown in Figure F.29. The simulation was performed for 1,000,000 iterations, saving output every 5,000 iterations. Five permeability values at the end of of the simulation (equivalent to 25,000 LB iterations) are fitted with a function $\kappa(t) = ae^{-bt} + c$, where t is the LB simulation time step. The value of the coefficient c ($3233mD$) is used as the permeability of this synthetic sample at infinite simulation time.

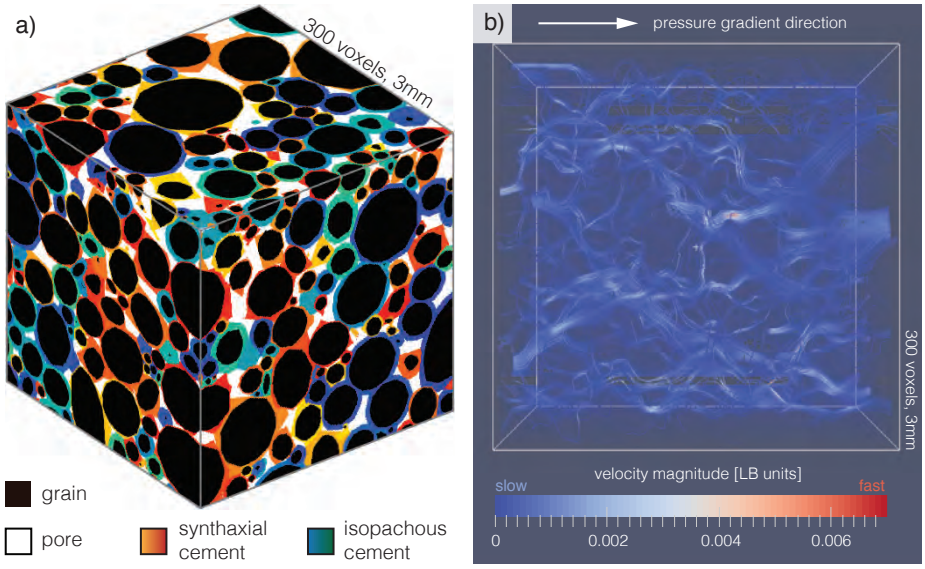

Figure F.31: a) A model output of Calcite3D with the crystal form $01\bar{1}2$ ($\alpha_v = 66.3\%$, $\beta = 5$ voxel, $\phi = 12.4\%$); b) the magnitude of velocity is displayed along streamlines; the flow was simulated through the model output shown in (a) using the Lattice Boltzmann method and the resulting permeability is $\kappa = 850mD$.

of permeability is assumed and permeability is extrapolated using a formula: $\kappa(t) = ae^{-bt} + c$, where t is the LB simulation time step, and the coefficient c gives the value of the permeability at infinite time.

References

[1] D. A. Budd, Permeability loss with depth in the cenozoic carbonate platform of west-central florida, AAPG Bulletin 85 (7) (2001) 1253–1272. arXiv:http://aapgbull.geoscienceworld.org/content/85/7/1253.full.pdf+html, doi:10.1306/8626CAAF-173B-11D7-8645000102C1865D.
URL http://aapgbull.geoscienceworld.org/content/85/7/1253.abstract

[2] C. van der Land, R. Wood, K. Wu, M. I. van Dijke, Z. Jiang, P. W. Corbett, G. Couples, Modelling the permeability evolution of carbonate rocks, Marine and Petroleum Geology 48 (2013) 1 – 7. doi:http://dx.doi.org/10.1016/j.marpetgeo.2013.07.006.
URL http://www.sciencedirect.com/science/article/pii/S0264817213001748

[3] Z. Liang, M. Ioannidis, I. Chatzis, Permeability and electrical conductivity of porous media from 3d stochastic replicas of the microstructure, Chemical Engineering Science 55 (22) (2000) 5247 – 5262. doi:http://dx.doi.org/10.1016/S0009-2509(00)00142-1.
URL http://www.sciencedirect.com/science/article/pii/S0009250900001421

[4] S. Roth, B. Biswal, G. Afshar, R. J. Held, P.-E. Øren, L. Inge Berge, R. Hilfer, Continuum-based rock model of a reservoir dolostone with four orders of magnitude in pore sizes, AAPG Bulletin 95 (6) (2011) 925–940. arXiv:http://aapgbull.geoscienceworld.org/content/95/6/925.full.pdf+html, doi:10.1306/12031010092.

URL http://aapgbull.geoscienceworld.org/content/95/6/925.abstract

[5] H. Okabe, M. J. Blunt, Pore space reconstruction of vuggy carbonates using microtomography and multiple-point statistics, Water Resources Research 43 (12) (2007) n/a–n/a. doi:10.1029/2006WR005680.
URL http://dx.doi.org/10.1029/2006WR005680

[6] B. Biswal, P. E. Øren, R. J. Held, S. Bakke, R. Hilfer, Stochastic multiscale model for carbonate rocks, Physical Review E 75 (6) (2007) 061303–.
URL http://link.aps.org/doi/10.1103/PhysRevE.75.061303

[7] M. A. Mousavi, M. Prodanovic, D. Jacobi, New classification of carbonate rocks for process-based pore-scale modeling, Society of Petroleum Engineersdoi:10.2118/163073-PA.

[8] S. Harland, R. Wood, A. Curtis, M. van Dijke, K. Stratford, Z. Jiang, W. Kallel, K. Sorbie, Quantifying flow in variably wet microporous carbonates using object-based geological modelling and both lattice-boltzmann and pore network fluid flow simulations, AAPG Bulletin.

[9] R. Lander, R. Larese, L. Bonnell, Toward more accurate quartz cement models: The importance of euhedral versus noneuhedral growth rates, AAPG Bulletin 92 (11) (2008) 1537–1563.
URL http://aapgbull.geoscienceworld.org/cgi/content/abstract/92/11/1537

[10] F. Lucia, Carbonate Reservoir Characterization An Integrated Approach, 2nd Edition, Springer, 2007.

[11] J. E. Neilson, N. H. Oxtoby, M. D. Simmons, I. R. Simpson, N. K. Fortunatova, The relationship between petroleum emplacement and carbonate reservoir quality: examples from abu dhabi and the amu darya basin, Marine and Petroleum Geology 15 (1) (1998) 57 – 72. doi:http://dx.doi.org/10.1016/S0264-8172(97)00033-0.

URL http://www.sciencedirect.com/science/article/pii/S0264817297000330

[12] A. C. Knoerich, M. Mutti, Epitaxial calcite cements in earth history: a cooler-water phenomenon during aragonite-sea times?, Geological Society, London, Special Publications 255 (1) (2006) 323–335. arXiv:http://sp.lyellcollection.org/content/255/1/323.full.pdf+html, doi:10.1144/GSL.SP.2006.255.01.19.
URL http://sp.lyellcollection.org/content/255/1/323.abstract

[13] C. Moore, Carbonate Diagenesis and Porosity, 2nd Edition, Elsevier, 1989.

[14] T. Scoffin, An Introduction to Carbonate Sediments and Rocks, Blackie, 1987.

[15] K. Walker, D. Jernigan, L. Weber, Petrographic criteria for the recognition of marine, syntaxial overgrowths, and their distribution in geologic time, Carbonates and Evaporites 5 (2) (1990) 141–152. doi:10.1007/BF03174845.
URL http://dx.doi.org/10.1007/BF03174845

[16] W. Ahr, Geology of Carbonate Reservoirs: The Identification, Description, and Characterization of Hydrocarbon Reservoirs in Carbonate Rocks, Wiley, 2008.

[17] M. Tucker, V. Wright, Carbonate Sedimentology, Blackwell Science, 1990.

[18] E. Flügel, Microfacies of Carbonate Rocks Analysis, Interpretation and Application, Springer, 2010.

[19] J. Mullin, Crystallization, fourth edition, Butterworth Heinemann, 2001.

[20] J. Dickson, Graphical modelling of crystal aggregates and its relevance to cement diagnosis, Philosophical Transactions of the Royal Society of London. Series A, Mathematical and Physical Sciences 309 (1509) (1983) 465–502.

URL http://rsta.royalsocietypublishing.org/content/309/1509/465.abstract

[21] A. Kelly, K. Knowles, Crystallography and Crystal Defects, Wiley, 2012.

[22] F. Massaro, L. Pastero, M. Rubbo, D. Aquilano, Theoretical surface morphology of 01(1)2 acute rhombohedron of calcite - a comparison with experiments and 10(1)4 cleavage rhombohedron, Journal of Crystal Growth.

[23] M. E. Tucker, R. G. C. Bathurst (Eds.), Carbonate Diagenesis, Blackwell Publishing Ltd., 2009.

[24] K. Bjorlykke, Petroleum Geoscience From Sedimentary Environments to Rock Physics Petroleum Geoscience From Sedimentary Environments to Rock Physics, Springer, 2010.

[25] A. Lønøy, Making sense of carbonate pore systems, AAPG Bulletin 90 (9) (2006) 1381–1405.
URL http://aapgbull.geoscienceworld.org/content/90/9/1381.abstractN2-Themostwidelyusedpore-typeclassificationsystemsforcarbonatereservoirsarelimitExistingclassificationschemesforporosity-permeabilitydatadonot,inmanycases,optimallyintegratesedimentology,diagenesis,andflow-relatedproperties.Inmanycarbonatereservoirs,itisthereforedifficulttogeneratepredictivemodelsforreservoir-qualitydistribution,resultinginsignificantuncertaintyinhydrocarbonreservecalculations.Basedonempiricaldata,mostlyfromEuropeandtheMiddleEast,anewpore-typeclassificationsystemhasbeendeveloped.Thenewsystemnotonlyuseselementsfromexistingpore-typeclassificationsystems,butalsointroducesmanynewelements.Thenewpore-typesystemincludes20pore-typeclassesthatshowItcombinessedimentologicanddiageneticfeatureswithflow-relatedproperties,andreservoir-criticalparameterscanthusbepredictedusingsedimentologicanddiageneticmodels.ApracticalexamplebasedondatafromaDevonianhydrocarbonfieldshowsthatpore-typevariationsmay

[26] N. P. James, B. Jones, Origin of Carbonate Sedimentary Rocks, Wiley, 2015.

[27] E. Coumans, Bullet 2.83 Physics SDK Manual, bulletphysics.org (2015).

[28] Blender Foundation, Blender Institute, Amsterdam, Blender - a 3D modelling and rendering package (2015).

[29] S. Chen, G. D. Doolen, Lattice Boltzmann Method for Fluid Flows, Annual Review of Fluid Mechanics 30 (1) (1998) 329–364.
URL http://arjournals.annualreviews.org/doi/abs/10.1146%2Fannurev.fluid.30.1.329

[30] X. Zhang, A. G. Bengough, J. W. Crawford, I. M. Young, A lattice BGK model for advection and anisotropic dispersion equation, Advances in Water Resources 25 (1) (2002) 1 – 8. doi:10.1016/S0309-1708(01)00047-1.
URL http://www.sciencedirect.com/science/article/pii/S0309170801000471

[31] J. Ma, K. Wu, Z. Jiang, G. D. Couples, SHIFT: An implementation for lattice Boltzmann simulation in low-porosity porous media, Physical Review E 81 (2010) 056702. doi:10.1103/PhysRevE.81.056702.
URL http://link.aps.org/doi/10.1103/PhysRevE.81.056702

[32] Q. Kang, P. C. Lichtner, D. R. Janecky, Lattice Boltzmann Method for Reacting Flows in Porous Media, Advances in Applied Mathematics and Mechanics 2 (5) (2010) 545–563. doi:{10.4208/aamm.10-10S02}.

[33] E. S. Boek, M. Venturoli, Lattice-Boltzmann Studies of Fluid Flow in Porous Media with Realistic Rock Geometries, Computers & Mathematics with Applications 59 (7) (2010) 2305–2314. doi:10.1016/j.camwa.2009.08.063.
URL http://dx.doi.org/10.1016/j.camwa.2009.08.063

[34] S. Mahmoudi, A. Hashemi, S. Kord, Gas-liquid relative permeability estimation in 2d porous media by lattice boltzmann method: Low viscosity ratio 2d lbm relative permeability, Iranian Journal of Oil & Gas Science and Technology.

[35] B. Ahrenholz, J. Tölke, P. Lehmann, A. Peters, A. Kaestner, M. Krafczyk, W. Durner, Prediction of capillary hysteresis in a porous material using lattice-boltzmann methods and comparison to experimental data and a morphological pore network model, Advances in Water Resources 31 (9) (2008) 1151 – 1173, quantitative links between porous media structures and flow behavior across scales. doi:http://dx.doi.org/10.1016/j.advwatres.2008.03.009.
URL http://www.sciencedirect.com/science/article/pii/S0309170808000511

[36] E. Coon, M. Porter, Q. Kang, Taxila lbm: a parallel, modular lattice boltzmann framework for simulating pore-scale flow in porous media, Computational Geosciences 18 (1) (2014) 17–27. doi:10.1007/s10596-013-9379-6.
URL http://dx.doi.org/10.1007/s10596-013-9379-6

[37] M. Zhang, G. Ye, K. van Breugel, Microstructure-based modeling of permeability of cementitious materials using multiple-relaxation-time lattice boltzmann method, Computational Materials Science 68 (0) (2013) 142 – 151. doi:http://dx.doi.org/10.1016/j.commatsci.2012.09.033.
URL http://www.sciencedirect.com/science/article/pii/S0927025612005915

[38] M. Halisch, Application and assessment of the lattice boltzmann method for fluid flow modeling in porous rocks, Ph.D. thesis, Technischen Universität Berlin (2013).

[39] M. Zalzale, Water dynamics in cement paste: insights from lattice boltzmann modelling, Ph.D. thesis, École Polytechnique Federeale de Lausanne (2014).

[40] S. Bakke, P.-E. Øren, 3-d pore-scale modelling of sandstones and flow simulations in the pore networks, Society of Petroleum Engineersdoi:10.2118/35479-PA.

[41] M. A. Seaton, R. L. Anderson, S. Metz, W. Smith, DL_MESO: highly scalable mesoscale simulations, Molecular Simulation 39 (10) (2013) 796–821. doi:10.1080/08927022.2013.772297.
URL http://dx.doi.org/10.1080/08927022.2013.772297

[42] F. G. Helfferich, Principles of adsorption and adsorption processes, AIChE Journal 31 (3) (1985) 523–524. doi:10.1002/aic.690310335.
URL http://dx.doi.org/10.1002/aic.690310335

[43] F. J. Lucia, Rock-fabric/petrophysical classification of carbonate pore space for reservoir characterization, AAPG Bulletin 79 (9) (1995) 1275–1300.
URL http://aapgbull.geoscienceworld.org/content/79/9/1275.short

[44] S. E. Melzer, D. A. Budd, Retention of high permeability during shallow burial (300 to 500 m) of carbonate grainstones, Journal of Sedimentary Research 78 (8) (2008) 548–561. arXiv:http://jsedres.sepmonline.org/content/78/8/548.full.pdf+html, doi:10.2110/jsr.2008.060.
URL http://jsedres.sepmonline.org/content/78/8/548.abstract

[45] P. Enos, L. H. Sawatsky, Pore networks in holocene carbonate sediments, Journal of Sedimentary Research 51 (3) (1981) 961–985. arXiv:http://jsedres.sepmonline.org/content/51/3/961.full.pdf+html, doi:10.1306/212F7DF1-2B24-11D7-8648000102C1865D.
URL http://jsedres.sepmonline.org/content/51/3/961.abstract

[46] D. Legland, geom3d, Matlab Central File Exchange, http://uk.mathworks.com/matlabcentral/ fileexchange/24484-geom3d, 20.05.2015.

[47] B. Silverman, Density Estimation for Statistics and Data Analysis, Springer, 1986.

[48] D.-J. Kroon, Wavefront OBJ toolbox, Matlab Central File Exchange, http://ch.mathworks.com/matlabcentral/fileexchange/27982-wavefront-obj-toolbox, 09.09.2011.

[49] J. D'Errico, Inhull, Matlab Central File Exchange, http://ch.mathworks.com/matlabcentral/fileexchange/10226-inhull, 06.09.2012.

[50] D.-J. Kroon, Patch Normals, Matlab Central File Exchange, http://uk.mathworks.com/matlabcentral/fileexchange/24330-patch-normals, 02.06.2009.

[51] Q. Zou, X. He, On pressure and velocity boundary conditions for the lattice boltzmann bgk model, Physics of Fluids (1994-present) 9 (6) (1997) 1591–1598.
URL http://scitation.aip.org/content/aip/journal/pof2/9/6/10.1063/1.869307

[52] A. Narváez, T. Zauner, F. Raischel, R. Hilfer, J. Harting, Quantitative analysis of numerical estimates for the permeability of porous media from lattice-Boltzmann simulations, Journal of Statistical Mechanics: Theory and Experiment 2010 (11) (2010) P11026.
URL http://stacks.iop.org/1742-5468/2010/i=11/a=P11026